

Surface wave interactions with submerged horizontal viscoelastic sheets

Dharma Sree K. K.¹, Sourav Mandal², and Adrian Wing-Keung Law^{1,3*}

¹Environmental Process Modelling Centre, Nanyang Environment and Water Research Institute (NEWRI), Nanyang Technological University, 1 CleanTech Loop, CleanTech One, #06-08, Singapore 637141

²Ocean Engineering Division, CSIR-National Institute of Oceanography, Goa, India

³School of Civil and Environmental Engineering, Nanyang Technological University, 50 Nanyang Avenue, Singapore 639798

*Corresponding author: dharma.sree@ntu.edu.sg

Abstract

In this study, the surface wave interactions with submerged horizontal viscoelastic sheets of varying rheological properties are investigated both experimentally and analytically. In the experiments, we adopt the novel development in preparing finite length viscoelastic sheets with different rheological properties using oil-doped polydimethylsiloxane (PDMS) materials reported earlier in Sree et al. (2017, 2018). The wave interactions with the submerged viscoelastic sheets are quantified using ultrasonic sensors at different locations in terms of the reflection and transmission behavior. The experimental results show that the wave-sheet interactions are complex. The wave pattern at the submerged sheet region significantly depends on its rheological properties. For larger submergence, a standing wave pattern with primarily lower order modes develops along the sheet with a significant reduction of transmitted wave energy past the sheet region for shorter period waves. An almost complete cutoff (up to 99% reduction in wave energy transmission) occurs with the flexible sheet held close to the mean water level (MWL), while 50-90% reduction in wave energy transmission is recorded with the stiffer sheets. An analytical study is also carried out under the assumption of small amplitude water wave theory. The sheet is modeled based on the viscoelastic representation of the Voigt model and the analytical problem is solved using the domain matching technique. The profiles of surface wave as well as sheet displacement are well predicted by the analysis compared to the experimental measurements. However, the displacement amplitude is underestimated due to the fixed end conditions assumed. The predicted dispersion relation for the surface waves also agrees well with the experimental results for the shorter period waves, however larger discrepancies are observed with longer wave periods. In addition, the experimental results are up to one order of magnitude higher with respect to wave reflection. Thus, further improvement is needed in the future for the analysis to better represent the surface wave interactions with submerged viscoelastic sheets.

Keywords: viscoelastic, submerged sheet, dispersion relation, wave reflection, wave transmission

1. Introduction

Coastal protection is a subject of national interest to many countries around the globe. In recent years, there has also been a significant increase in research due to the ongoing threat of climate changes and sea level rise which can increase the incident wave energy to the shore. Various protective measures have been proposed in the past, and the approach of floating breakwaters has received much attention due to their flexibility in installation (even with poor soil conditions). They are deemed particularly effective in relatively calm coastal waters within sheltered regions (Dai et al., 2018), and have lesser impact to the ecological conditions since they do not interfere significantly with the tidal exchanges.

In the literature, floating breakers of both voluminous caisson-type (e.g. He et al., 2012 and 2013) and thin plate-type (e.g. Yang et al., 2012) have been examined previously. For the thin plate-type floating breakwaters, almost all previous studies assumed solid plates with an elastic representation for the constitutive behavior of the material. Thus, the configuration is akin to the well-known field of hydroelasticity for large floating platforms (Ohkusu and Namba, 2004) that has been investigated extensively. Despite their advantages, floating plate-type breakwaters remain an obstruction to the natural sea view, which can be an important consideration for recreational or residential shore development. An alternative is thus to moor the plates below the water level to act as submerged breakwaters to reduce the wave transmission behind. The idea of submerged horizontal plates as wave dampers was initially examined by Heins (1950) analytically based on the configuration of a semi-infinite plate in finite water depth. The work was later extended to infinite water depth by Greene and Heins (1953). Subsequently, Burke (1964), and Siew and Hurley (1977) considered finite rigid plates in deep waters and shallow waters, respectively. Patarapanich (1984) extended the analytical investigation over a wide range of ambient conditions from deep to shallow waters using the finite element method. His study also established the relationship linking the incident waves and plate dimensions to the reflected and transmitted wave characteristics.

In terms of laboratory studies, Patarapanich and Cheong (1989) performed experiments using marine plywoods as submerged horizontal plates, to investigate the optimum conditions for maximum reflection and minimum transmission based on the plate length to wavelength ratio as well as water depth ratio. They found that the minimum transmission was not always associated with the maximum reflection, because the energy loss due to wave breaking may play an important role. Neelamani and Reddy (1992) carried out experiments using perspex glass plates instead. Their results showed that the submerged plate can act as an excellent shore protection measure, with maximum reflection occurring when the rigid plate is fixed at the water surface and maximum

energy loss when submerged at a shallow depth. Recent studies also examined other configurations, including multiple plates stacked with gaps in between. In these studies, rigid plates with large elastic modulus, namely aluminum (Fang et al., 2018), acrylic (Liu and Li, 2014), and stainless steel (Cho et al., 2013) plates, were typically adopted and their high rigidity and small deformation can be neglected in the wave interaction analysis.

With submerged elastic plates, Hassan et al. (2009) examined analytically the wave interactions for finite length and negligible thickness using the linear wave theory and solved the dispersion relation using the domain matching method. William and Meylan (2012) also investigated the same configuration analytically but using the technique of Wiener–Hopf and residue calculus instead. Besides reducing the wave transmission, Renzi (2016) proposed that the deformation of the submerged horizontal elastic plates due to the wave action can also be used to produce electricity with piezoelectric wave energy converters. Buriani and Renzi (2017) extended the piezoelectric concept to submerged horizontal elastic plates having one end fixed to shoreline seawalls. Mohapatra et al. (2018a) considered the structural response of submerged horizontal flexible plates under wave action to act as heave plates. The study was also extended to include porosity for the submerged flexible plates (2018b).

With negligible rigidity, the submerged plate would behave as a membrane instead with the magnitude of induced displacement comparable to the wave amplitude. Cho and Kim (1998; 1999) predicted analytically that a horizontal elastic membrane can effectively act as a wave barrier with an optimal combination of design parameters, the performance of which depends significantly on its flexibility. Later, Cho and Kim (2000) investigated the same configuration but with the addition of small porosity to the membrane. Recently, Shugan et al. (2012) studied the performance of an elastic thin plate with fixed edges as the floating breakwater. They also found that the wave-blocking efficiency can be substantially improved using flexible sheets with lower elasticity.

In terms of field applicability, the use of flexible sheets in coastal applications has become widespread over the years. For example, reinforced rubber sheets (such as geotextile and geosynthetic tubes) as well as reinforced woven geotextile fabric (such as silt curtains in coastal waters) are now commonly adopted due to the significant advancement in the material research (Northwest Lining and Geotextile, 2018). Thus, they can also be realistic alternatives for the installation of submerged horizontal sheets in field conditions. The constitutive behavior for these materials (e.g. reinforced rubber material in Popov et al. (2019) and reinforced woven geotextile fabric in Kim and Kee (1996, 1997)) is typically viscoelastic, with the elastic properties linking the imposing forces to deformations directly while the material energy dissipation is accounted for using

the viscosity parameter. As discussed above, all previous studies had adopted the elastic assumption for the submerged plates and sheets, and no viscoelastic representation for the analysis can be found in the literature so far.

To address the research gap, we investigate the surface wave interactions with submerged horizontal viscoelastic sheets both experimentally and analytically in the present study. A novel technique is adopted in preparing finite length viscoelastic sheets with different rheological properties for the experiment, using oil-doped polydimethylsiloxane (PDMS) materials reported earlier in Sree et al. (2017, 2018). The wave interactions with the submerged viscoelastic sheets are then measured using ultrasonic sensors at different locations along the wave flume to quantify the reflection and transmission behavior. In addition, we also carry out an analytical analysis using the linear wave theory with domain matching, and the predictions are compared with the experimental measurements.

The outline of the paper is as follows: Section 2 describes the preparation of viscoelastic sheets in the laboratory as well as the quantification of their mechanical properties. Section 3 presents the experimental setup for the experiments with surface wave interactions, and the ultrasonic sensor measurements for wave modulation between the open water and submerged horizontal sheet region. The experimental results are analyzed in Section 4. Section 5 then shows the analytical analysis with the formulation of the viscoelastic dispersion relation as a direct outcome. Section 5 also compares the experimental results with the analytical predictions and discusses the comparison. Finally, the findings of the present study are summarized.

2. Viscoelastic material preparation and testing

The submerged viscoelastic sheets in the laboratory are made of oil-doped PDMS material (Sree et al., 2017, 2018), with standard dimensions of $1.0\text{m} \times 0.3\text{m} \times 0.01\text{m}$. The main components for the preparation are the prepolymer elastomer base and curing agent (which together is commercially available as Sylgard 184 Silicone Elastomer kit) and white oil. Since the mechanical characteristics of reinforced rubber or geotextile material can vary over a wide range, we aim for neutrally buoyant sheets with varying viscoelastic properties in the experiments as the first attempt. With the PDMS density being greater than water by itself, the oil doping is thus needed to achieve the near neutral buoyancy.

The preparation of the PDMS sheets involved three main steps: mixing the components, degassing and curing. The mass percentages of oil and curing agent can be defined respectively as follows:

$$m_o (\%) = \frac{M_o}{M_o + M_{CA} + M_B} \quad (1)$$

$$m_{CA} (\%) = \frac{M_{CA}}{M_{CA} + M_B} \quad (2)$$

where M_o , M_{CA} and M_B represent the mass of white oil, curing agent, and base respectively. In the present experiments, m_o is maintained at 5%, while the viscoelastic properties of the laboratory sheets are varied by setting m_{CA} to be 4%, 7%, and 10%. The oil-doped PDMS sheets are first prepared in-situ in steel trays, and then left to cure for one week at room temperature without any disruption. Subsequently, they are tested using oscillatory shears using a rheometer (Anton Paar, MCR 302, Germany) with a parallel plate geometry (PP20).

In the literature, viscoelastic representations can be broadly classified based on either the Voigt or Maxwell model. The Voigt model has a parallel combination of spring and dashpot, whereas the Maxwell model has series combination. The constitutive behavior between the stress and strain/strain rate for the Voigt model is given by:

$$\tau = G\gamma + \mu \frac{d\gamma}{dt} \quad (3)$$

while that for the Maxwell model is

$$\frac{d\gamma}{dt} = \frac{\tau}{\mu} + \frac{1}{G} \frac{d\tau}{dt} . \quad (4)$$

where τ is the shear stress, γ the deformation, G shear modulus, μ the dynamic viscosity and t the time. In both models, the coefficients representing the spring, G and dashpot μ are assumed to be constants.

Correspondingly, the storage modulus G' and loss modulus G'' can also be defined. For the Voigt model, the relationships are:

$$G' = G, \text{ a constant}; \quad G'' = \omega\mu \quad (5)$$

and for the Maxwell model, the relationships are

$$G' = \frac{G\xi_r^2\omega^2}{1+\xi_r^2\omega^2}; \quad G'' = \frac{G\xi_r\omega}{1+\xi_r^2\omega^2}. \quad (6)$$

where $\xi_r = \mu/G$ is the relaxation time.

During the oscillatory shear testing, the oil-doped PDMS sheet is subjected to an angular frequency ω and a given maximum strain (frequency sweep), and the resistance torque is measured to calculate the storage modulus G' and loss modulus G'' . With the Voigt model, G' would remain constant during the frequency sweep, while G'' would increase linearly with ω resulting in a constant dynamic viscosity μ . On the other hand, the Maxwell model has a very different behavior, with G' increasing with ω and approaching an asymptote when $\omega > 1/\xi$, while G'' increases with ω to a maximum at $\omega = 1/\xi$ then decreases.

The measurements of rheological properties with oscillatory frequency is shown in Fig. 1. The required frequency range is determined by equating the wave frequencies (σ) used in the experiments with the angular frequencies (ω) of the oscillatory shear tests. From the figure, it is evident that the constitute behavior of the PDMS sheets in the present experiments are close to the Voigt model with G' nearly constant and G'' monotonically increasing with frequency. The same conclusion was drawn in Sree et al. (2017, 2018) although the previous studies used a much higher percentage of the white oil ($m_o = 30\%$, compared to 5% in this study) for floating viscoelastic covers.

Fig. 1 also shows the variation of the rheological properties of the oil-doped PDMS sheets with time. Three samples are tested for each sheet with the specific m_{CA} , to confirm the repeatability of results. From the figure, it is evident that after the first week of curing, the rheological properties remain stable for another two weeks. Hence, all the wave experiments are performed within this stable two-week period. Based on the wave frequencies in the present experiments, the rheological results of the viscoelastic sheets can be obtained in Table 1 based on the Voigt model. It can be observed that the sheets become stiffer generally with a higher m_{CA} from 4 to 10 %, with corresponding larger G' but smaller G''/G' . When m_{CA} is increased from 4 to 7%, G' and G'' increase by 2.8 and 2.5 times, respectively. Further increasing m_{CA} to 10% leads to a bigger change, with the values of G' and G'' being 7.8 and 5.7 times that of $m_{CA} = 4\%$, respectively.

3. Experimental setup

The laboratory experiments are carried out in a wave flume as shown in Fig. 2. The flume is made of tempered transparent glass panels, with dimensions [length L , width B , depth D] = [8, 0.3, 1] m. It is filled with fresh water to a depth, $h = 0.3$ m. The wave flume is equipped with a piston-

type wave generator at one end and inclined mesh type wave absorber beach (Slope 1V:1.25H) at the other end. The wave generator can produce regular waves as well as irregular waves, however only regular wave experiments are performed in this study. A mesh-type vertical upstream absorber is installed behind the wave generator to absorb the energy of standing waves formed in this part of the flume.

In all experiments, the viscoelastic sheet is held at 2.6 m from the mean position of the piston. Three submergence depths are considered for the sheet: $H_s = 0.10, 0.075, \text{ and } 0.05$ m. The sheet submergence maintained by clamping both the leading and trailing edges of the sheet with bottom horizontal brackets that are fixed to the stainless-steel vertical stopper rods (0.8 cm diameter) attached to the wave flume framework, as illustrated in Fig. 2. Together, they prevent the overall surge or drift of the sheet along with the progressive waves. However, we note that there is small yielding of movement at the two edges during the wave cycle, such that a horizontal stretching of the sheet with overall tension would not occur. This arrangement mimics the field installation with anchors in a simplified manner, because the anchors would prevent the overall surge or drift of the sheet but would not be able to maintain a net tension unless a firm foundation is provided. The actual movement in the field installations is of course very complicated and will require a full-scale hydroelastic modelling of the anchor configuration to emulate (e.g. Sun et al., 2018).

The wave conditions for the experiments are provided in Table 2, where k_o is the wavenumber and A_0 is the wave amplitude in open water. Six wave periods are tested: $T = 0.5, 0.6, 0.7, 0.8, 0.9$ and 1.0 s. A static calibrated capacitance wave gauge is installed near the wave generator to control the stroke of the piston to produce incident waves of the required amplitude. Six ultrasound (US1 to US6) sensors (Ultra lab 40D, General Acoustics, Germany) are installed inside the wave flume also shown in Fig. 2. They have a resolution of 0.18 mm and sampling frequency of 50 Hz. US1 is fixed above the open water at 60 cm from the leading edge of the submerged sheet towards the piston, while US4 is above the open water behind at 20 cm from its trailing edge. US2/US3 and US5/6 are at a down-wave distance of 20/40 cm from US1 and US4, respectively. The synchronized data from all the ultrasound sensors are recorded with the software, LABVIEW, using a common data acquisition system (NI 9215, National Instruments, Texas). Sample results of these data are shown in Fig. 3.

The repeatability of the measurements is checked by performing each experimental condition at least three times. Thus, for each of the three viscoelastic sheets, a total of 54 experiments (i.e. 6 wave periods \times 3 repetitions \times 3 submergence) are performed. In addition, video recordings of the wave experiments are also taken using a high-resolution camera (1080 \times 1920 pixels) at a rate of 30

frames/second. The digitization of the videos is then carried out for the analysis which shall be discussed in next section. We note that the steel support frame of the wave flume restricted the viewable area in the video recordings to extend only from $x = 30$ to 100 cm ($x = 0$ cm at the leading edge of the viscoelastic sheet).

4. Experimental Results and Analysis

The results from both ultrasound sensors and video camera recordings are analyzed in the present study using the mathematical functions available in the MATLAB library. Only the first three fully developed waves (boxed portion shown in Fig. 3a, b and c) are considered in the analysis in order to avoid the effect of reflected waves from the beach. This transient approach has been well adopted previously (e.g. Law 1999, Huang and Law 2013, Sree et al. 2017, 2018).

For the ultrasound measurements, we first increase the data rate from 50 Hz to 200 Hz through the use of numerical interpolation with the *pchip* function (Piecewise Cubic Hermite Interpolating Polynomial) in MATLAB, which enables the identification of sharper wave crests and troughs. Spectral analysis is also carried out on the time series data using the discrete Fourier transform in MATLAB. The normalization of amplitude at each frequency is performed by dividing the value by the length of the signal, while the absolute value is considered to determine the amplitude of the double-sided wave spectrum $|H(\sigma)| = \text{abs}\{\text{fft}(\eta)\}/L$. In addition, the double-sided spectrum is shifted to adjust for the mean zero position using the function *fftshift()*, and only the single-sided amplitude spectrum is considered. The corresponding energy spectrum can be calculated as $\widetilde{E}_w = \left| \frac{E_w}{\rho g} \right| = \frac{(2|H(\sigma)|)^2}{2}$, see Fig. 4.

The video recordings are also analyzed using MATLAB. They are first converted into digital images using the *VideoReader()* and *read()* functions. The RGB images obtained are then converted into grey scale using the *rgb2gray()* function, and the intensity is adjusted using the *imadjust()* function which enables the digitization of images based on pixel brightness (also known as pixel value). Fig. 5 shows the sample results of the image frame and corresponding digitized data.

4.1 Dispersion relationship

The displacement lag Δx between two consecutive profiles with time difference Δt is shown in Fig. 6. It is obtained by the cross-correlation method by assuming that the waves considered are progressive. With the displacement lag, the wave celerity or phase velocity can then be calculated as:

$$c_p = \frac{\Delta x}{\Delta t} \quad (7)$$

The time series of the surface displacement at different locations along the submerged sheet region are analyzed using spectral analysis. With the deepest submergence $H_s = 0.10$ m, the results show a typical single peak frequency in the energy spectrum which corresponds to the incident wave frequency ($2\pi/T$). The celerity along the submerged sheet region can then be calculated based on the distance between the sensors and the time lag, and the corresponding wave number as $k = c_p \times T$.

The variation of wavenumber with wave period for the three sheets are provided in Fig. 7, where k_v^+ is the dominant wave number for viscoelastic plate covered region S_{22} . For comparison, the open water wavenumber based on the linear wave theory without sheet for the two water depths, $h = 0.3$ m (actual water depth) and $h = H_s$ (submergence) is also provided in the figure. For the shorter waves ($T < 0.7$ s), the surface water wavenumber along the submerged sheet region generally overlaps with the open water wavenumber without sheet. This illustrates that the submergence ratio $\frac{H_s}{\lambda}$ is sufficiently large so that the sheet conforms to the small orbital displacement of the progressive wave at the bottom and thus its presence does not alter the dispersion relation significantly. With the longer waves ($T > 0.7$ s), the open water dispersion relation for $h = 0.3$ m remains valid for the flexible sheet with $m_{CA} = 4\%$. However, when the sheet stiffness increases further, i.e. $m_{CA} = 7\%$, the wavenumber increases and eventually match well with the condition of $h = H_s$ when $m_{CA} = 10\%$.

4.2 Wave reflection

As mentioned before, Fig. 4 shows the comparison of energy spectra at the various locations along the wave flume. In particular, the spectra of the three ultrasound measurements US1, US2 and US3 are indicative of the magnitude of the wave reflection by the submerged sheet. If the reflection is negligible, the three spectra would then have the same peak intensity as the incident wave spectrum. On the other hand, if the reflection is large, the peak intensity would be modified depending on the nodal position of the partial standing wave pattern in front of the leading edge. Based on the general interpretation, it can be observed qualitatively from the figure that the reflection is negligible for the deeper submergence of $H_s = 0.1$ m, while becomes prominent with the shallow submergences.

To quantify the reflection coefficient, we analyze the time series data for the first three fully developed waves from the ultrasound sensors US1, US2 and US3 in Fig. 8. The data are fitted with the linear travelling wave equation, as shown below, using least square fit.

$$\eta(x, t) = A_o \cos(k_o x - \omega t + \phi) + R_o \cos(k_R x + \omega t + \phi_R) \quad (8)$$

where A_o is the incident wave amplitude (Table 2), R_o is the reflected wave amplitude, k_R is the wavenumber for reflected wave, ϕ is the phase of the incident wave and ϕ_R is the phase of reflected wave such that the phase shift is given by $\phi_S = \phi - \phi_R$. The reflection coefficient at the leading edge of the sheet can then be calculated using the following formula:

$$C_r = \frac{R_o}{A_o} \quad (9)$$

The analysis of the reflection coefficient is plotted in Fig. 9. With the shortest wave period $T = 0.5$ s, maximum reflection is observed for the stiffest sheet $m_{CA} = 10\%$. This is followed by the flexible sheet $m_{CA} = 4\%$ with approximately half of the magnitude, while the minimum reflection occurs for the intermediate $m_{CA} = 7\%$. The concave trend demonstrates the nonlinearity involved. When the wave period increases to $T = 0.6$ s, the minimum occurs with $m_{CA} = 10\%$ instead and maximum with $m_{CA} = 7\%$, though the range is relatively small. For $T = 0.7$ s and 0.8 s, $m_{CA} = 10\%$ again yields the minimum reflection, while no discernable difference can be observed for the other two sheets. Finally, with $T = 0.9$ and 1.0 s, the wave reflection becomes somewhat independent of the sheet properties.

4.3 Wave transmission

The effectiveness of the submerged viscoelastic sheet for wave protection depends on how much of the incident wave energy is transmitted past the sheet region. This can be assessed by comparing the incident wave energy \tilde{E}_{wL} in the open water in front of the sheet (at the leading edge) with the wave energy behind the sheet (at the trailing edge), \tilde{E}_{wT} . The percentage of wave energy reduction is expressed as

$$r_e(\%) = \frac{\tilde{E}_{wL} - \tilde{E}_{wT}}{\tilde{E}_{wL}} \times 100 \% \quad (10)$$

The benchmark case for open water without the submerged sheet is provided in Table 3. As expected, the results show that that less than 5% of the incident wave energy is reduced, which can be attributed to the viscous shears by the surrounding tank walls (Sree et al. 2018). In the presence of submerged viscoelastic sheet, significant reduction in wave energy is recorded that varies from 15% up to 99% (or nearly no transmission) for different experimental configurations (Table 4). In

Fig. 2, the wave generator is on the right side of the submerged sheet; the waves thus travel from right to left. Using the same alignment, for the profile views as shown in Fig. 10a, b, and c, the leading edge is on the right side of the sheet and trailing edge on the left side

We note that the reduction in wave transmission due to the submerged viscoelastic sheet can be due to four main mechanisms: (1) reflection from the leading edge of the submerge sheet (due to radiation by the sheet displacement), (2) viscous energy dissipation by the sheet material, (3) energy dissipation in the boundary layers on top and bottom of the sheet, and (4) wave breaking (for shallow submergence). The first three mechanisms bear similarity to the reduction in wave transmission due to the presence of floating viscoelastic covers in Sree et al. (2018) in which case the boundary layer dissipation is in fact identified as the dominant mechanism. With submerged sheet, however, wave breaking can occur for shallow submergence, and the energy dissipation by wave breaking is typically very effective and can dominate over the others.

In the present experiments, for the deep submergence $H_s = 0.1$ m, the wave pattern in the submerged sheet region depends significantly on the rheological properties of the sheet. The measured wave interactions with the different sheets are complex, as evident in Fig. 10 a, b and c. With $T = 0.5$ s, progressive wave transmission occurs past the flexible sheet of $m_{CA} = 4\%$ with negligible wave reduction. When the sheet stiffness increases to $m_{CA} = 7\%$, a standing wave pattern begins to emerge along the submerged sheet region. With the stiffest sheet, $m_{CA} = 10\%$, almost full reflection occurs at the leading edge with negligible transmission. The large displacement near the leading edge as compared to trailing edge for the stiffest sheet also coincides with the higher reflection coefficient shown in Fig. 9. For $T = 0.6$ s, the minimum transmission is observed for $m_{CA} = 4\%$. At the other end, for $T = 0.7$ and 0.8 s, $m_{CA} = 10\%$ yields the maximum transmission ($\sim 80\%$). For even longer waves with $T = 0.9$ and 1.0 s, the wave transmission does not depend on the sheet properties anymore.

When the submergence is reduced to $H_s = 0.075$ m, for the shorter waves ($T = 0.5$ and 0.6 s), a standing wave pattern with primarily lower order modes develops along the flexible sheet ($m_{CA} = 4\%$) with a significant reduction of transmitted wave energy past the sheet region. The reduction further increases when the sheet stiffness increases to $m_{CA} = 7\%$. When the wave period increases to $T = 0.7$ and 0.8 s, higher order modes begin to be excited (see Fig. 10a). Beyond that, the standing wave pattern diminishes with further increase in the wave period to 0.9 to 1.0 s. The development illustrates again the complex interactions between the surface progressive waves and submerged sheet, which is dependent on the rheological properties. Overall, an important point to note is that the

presence of standing waves is typically associated with a significant reduction in the transmitted wave energy.

With the smallest submergence $H_s = 0.05$ m, we expect that the reduction in the wave energy transmission will be significantly enhanced by the stronger nonlinear wave interactions between the surface progressive wave and submerged sheet, as well as potential wave breaking at the water surface. This is indeed the case based on the experimental observations, as shown in Figs. 10 a, b and c, and Table 4. The significant reduction in wave energy transmission with the shallower submergence of the sheet is recorded for all combinations of waver periods and sheet characteristics. In other words, the performance of submerged sheet as breakwater is closely linked its submergence. In fact, we observe an almost complete cutoff (up to 99% reduction in wave energy transmission) with the flexible sheet $m_{CA} = 4\%$ held close to the mean water level (MWL). For the other two stiffer sheets with $m_{CA} = 7\%$ and 10% , 50-90% reduction in wave energy transmission is recorded when the sheet is held close to the MWL.

5. Analytical model

In the present study, we further examine the wave interaction with the submerged viscoelastic sheet analytically under the assumptions of linear wave theory and small amplitude sheet response. The problem is considered in Cartesian coordinate system as shown in Fig. 11, with water of finite depth h , finite viscoelastic sheet of length L_s , and submergence H_s . The leading edge of the submerged sheet is situated at $x = 0$, with z -axis being vertically upwards and $z = 0$ being the free surface. The fluid domain is divided into four regions, namely: (i) Region 1 (S_1): $-\infty < x < 0$; $-h \leq z \leq 0$, (ii) Region 2 (S_{21}): $0 \leq x \leq L_s$; $-H_s \leq z \leq 0$, (iii) Region 3 (S_{22}): $0 \leq x \leq L_s$; $-h \leq z < -H_s$, and (iv) Region 4 (S_3): $L_s < x < \infty$; $-h \leq z \leq 0$.

The fluid is assumed to be incompressible, inviscid and irrotational in time with angular frequency ω . Therefore, its motion can be fully described by a complex velocity potential of the form $\Phi_j(x, z, t) = Re\{\phi_j(x, z)e^{-i\omega t}\}$ where ϕ_j is the spatial velocity potential at the j^{th} region satisfying the following Laplace equation

$$\nabla^2 \phi_j = \left(\frac{\partial^2}{\partial x^2} + \frac{\partial^2}{\partial z^2} \right) \phi_j = 0, \quad j = 1, 21, 22, 3, \quad (11)$$

along with the linearized free surface boundary condition at $z = 0$,

$$\frac{\partial \phi_j}{\partial z} - K \phi_j = 0, \quad j = 1, 21, 3, \quad (12)$$

with $K = \omega^2/g$ where g being the acceleration due to gravity. The bottom boundary conditions at $z = -h$, are given by

$$\frac{\partial \phi_j}{\partial z} = 0, j = 1,2,3, \quad (13)$$

On the other hand, at the surface of the submerged viscoelastic sheet, the kinematic and dynamic conditions are given by

$$\frac{\partial \xi}{\partial t} = \frac{\partial \Phi_{21}}{\partial z} = \frac{\partial \Phi_{22}}{\partial z}, p_s = \rho \frac{\partial(\Phi_{22} - \Phi_{21})}{\partial t}, z = -H_s, \quad (14)$$

where the real value of $\xi(x, t) = \xi_0(x)e^{-i\omega t}$ being the submerged sheet displacement, ρ the fluid density and p_s the pressure acting across the sheet surface. It is assumed that the sheet is thin and of uniform thickness d_s , and made of homogenous viscoelastic material of mass density ρ_s . Introducing viscosity into the thin plate Euler-Bernoulli beam equation (Fox and Squire 1994, Mosig et al. 2015) with the small displacement assumption, the dynamic pressure acting on the submerged viscoelastic sheet can be written as:

$$p_s = \frac{G_v d_s^3}{6(1-\vartheta)} \frac{\partial^4 \xi}{\partial x^4} + \rho_s d_s \frac{\partial^2 \xi}{\partial t^2} \quad (15)$$

In Eq. (15), G_v is the complex Voigt shear modulus $G_v = G' - i\omega\nu$, ϑ the Poisson ratio and $\nu = G''/\omega$ the dynamic viscosity. Using Eqs. (11), (14) and (15), the boundary condition for the submerged viscoelastic sheet can be written as,

$$\left(\frac{G_v d_s^3}{6(1-\vartheta)} \frac{\partial^4}{\partial z^4} + \rho_s d_s \frac{\partial^2}{\partial t^2} \right) \frac{\partial \Phi_{22}}{\partial z} = \rho \frac{\partial^2(\Phi_{22} - \Phi_{21})}{\partial t^2} \quad (16)$$

The following sheet condition can be derived after further simplification of Eq. (16),

$$\frac{D}{Dz} \frac{\partial \phi_{22}}{\partial z} + K(\phi_{21} - \phi_{22}) = 0 \quad (17)$$

where $\frac{D}{Dz} \equiv \frac{D'}{\rho g} \frac{\partial^4}{\partial z^4} - \frac{m_s \omega^2}{\rho g}$, with $D' = \frac{G_v d_s^3}{6(1-\vartheta)}$ and $m_s = \rho_s d_s$. It is important to note that $\eta \rightarrow 0$ in Eq. (15) leads to a purely elastic thin beam. Therefore, simply replacing G_v by G' in Eq. (17), gives the boundary condition for the submerged thin elastic sheet.

The boundary conditions at the leading and trailing edges are the most difficult to handle. Small movements at these edges are almost inevitable in both the experimental and field conditions. Here, in order to obtain some analytical results for comparison, we assume that the edges are fixed, i.e. at $z = -H_s$, $x = 0$ and $x = L_s$,

$$\text{Fixed edge: } \frac{\partial^2 \phi_{22}}{\partial x \partial z} = 0, \quad \frac{\partial \phi_{22}}{\partial z} = 0 \quad (18)$$

Finally, the continuity of pressure and normal velocity near the interfaces yields,

$$\text{Region 1, 2 and 3: } \phi_1 = \begin{cases} \phi_{21}, & \frac{\partial \phi_1}{\partial x} = \begin{cases} \frac{\partial \phi_{21}}{\partial x}, & -H_s < z < 0, \\ \frac{\partial \phi_{22}}{\partial x}, & -h < z < -H_s, \end{cases} \end{cases} \text{ at } x = 0, \quad (19a)$$

$$\text{Region 2, 3 and 4: } \phi_3 = \begin{cases} \phi_{21}, & \frac{\partial \phi_3}{\partial x} = \begin{cases} \frac{\partial \phi_{21}}{\partial x}, & -H_s < z < 0, \\ \frac{\partial \phi_{22}}{\partial x}, & -h < z < -H_s, \end{cases} \end{cases} \text{ at } x = L_s, \quad (19b)$$

Applying the separation of variables method in the governing Eq. (11), and with the free surface boundary condition, bottom boundary condition and submerged sheet condition as in Eqs. (12), (13) and (17) respectively, the following expression of velocity potentials can be obtained:

$$\phi_1(x, z) = I_0 e^{ik_w,0x} \psi_{w,0}(z) + \sum_{n=0}^{\infty} R_n e^{-ik_w,nx} \psi_{w,n}(z), \quad x, z \in S_1, \quad (20a)$$

$$\phi_{2j}(x, z) = \sum_{n=I,II,0}^{\infty} (A_n e^{-ik_{v,n}x} + B_n e^{ik_{v,n}x}) \psi_{v,jn}(z), \quad x, z \in S_{2j}, \quad j = 1, 2, \quad (20b)$$

$$\phi_3(x, z) = \sum_{n=0}^{\infty} T_n e^{ik_w,nx} \psi_{w,n}(z), \quad x, z \in S_3, \quad (20c)$$

where $I_0 = -igH_0/(2\omega)$ with H_0 being the incident wave height.

The depth dependent eigenfunctions $\psi_{wn}(z)$ and $\psi_{vjn}(z)$ have the following forms:

$$\psi_{w,n}(z) = \frac{\cosh k_{w,n}(h+z)}{\cosh k_{w,n}h} \quad (21a)$$

$$\psi_{v,jn}(z) = \begin{cases} \sinh k_{v,n}(h - H_s) (k_{v,n} \cosh k_{v,n}z + K \sinh k_{v,n}z), & j = 1 \\ \cosh k_{v,n}(h + z) (K \cosh k_{v,n}H_s - k_{v,n} \sinh k_{v,n}H_s), & j = 2 \end{cases} \quad (21b)$$

The open water wave number $k_{w,n}$ satisfies the dispersion relation $\omega^2 = gk_{w,n} \tanh k_{w,n}h$, where $k_{w,0}$ is the real root and $k_{w,n}$ s ($n > 0$) are purely imaginary roots. On the other hand, the dispersion relation for the submerged sheet region is given by

$$KU = (UVk_{v,n} + KW) \tanh k_{v,n}(h - H_s) \quad (22a)$$

$$U = K \cosh k_{v,n}H_s - k_{v,n} \sinh k_{v,n}H_s \quad (22b)$$

$$W = k_{v,n} \cosh k_{v,n}H_s - K \sinh k_{v,n}H_s \quad (22c)$$

$$\rho g V = D'k_{v,n}^4 - m_s\omega^2 \quad (22d)$$

The dispersion relation Eq. (22) can be rewritten in the following form:

$$\omega_{\pm}^2 = g \frac{-B \pm \sqrt{B^2 - 4AC}}{2A}, \quad (23a)$$

where $A = (-m_s g k_{v,n} \cosh k_{v,n}H_s - \sinh k_{v,n}H_s) \sinh k_{v,n}(h - H_s)$

$$- \cosh k_{v,n}H_s \cosh k_{v,n}(h - H_s) \quad (23b)$$

$$B = \left(m_s g k_{v,n}^2 \sinh k_{v,n}H_s + D' k_{v,n}^5 \cosh k_{v,n}H_s \right) \sinh k_{v,n}(h - H_s) \\ + k_{v,n} \sinh k_{v,n}H_s \cosh k_{v,n}(h - H_s) \quad (23c)$$

$$C = -D' k_{v,n}^6 \sinh k_{v,n}H_s \sinh k_{v,n}(h - H_s) \quad (23d)$$

In Eq. (17), ω_+^2 and ω_-^2 are associated with the progressive wave mode in regions S_{22} and S_{21} , respectively. Thus, the dispersion relation in Eq. (22) has an infinite number of complex roots. However, only two roots will have larger real parts (k_v^- and k_v^+ with $k_v^- < k_v^+$) compared to the imaginary part, which are associated with the dominant wave number of S_{21} and S_{22} , respectively. To resolve these two dominant progressive wave numbers, the two relations in Eq. (23), are solved using Newton Raphson method, with $\psi_{w,n}(z)$ in Eqs. (20a, 20c) satisfying the following orthogonal relationships:

$$\langle \psi_{w,m}(z), \psi_{w,n}(z) \rangle = 0, \text{ (for } m \neq n) \quad (24a)$$

$$\langle \psi_{w,m}(z), \psi_{w,n}(z) \rangle = \int_{-h}^0 \psi_{w,m}^2(z) dz, \text{ (for } m = n) \quad (24b)$$

In Eqs. (20a) - (20c), the unknowns R_n, A_n, B_n and T_n s are to be determined by using Eq. (20) in prescribed interface boundary conditions.

Now, substituting ϕ_1 and ϕ_{2j} from Eqs. 20(a)-(b) in the continuity of pressure and normal velocity Equation 19(a) near the interfaces at $x = 0$, and using the orthogonality of $\psi_{w,m}(z)$, yield

$$(\delta_{0n}I_0 + R_n)a_n - \sum_{n=I,II,0}^{\infty}(A_n + B_n)b_n = 0, \quad (25a)$$

$$(\delta_{0n}I_0 - R_n)k_{w,n}a_n + \sum_{n=I,II,0}^{\infty}(A_n - B_n)k_{v,n}b_n = 0, \quad (25b)$$

where $a_n = \int_{-h}^0 \psi_{w,n}^2(z)dz$, $b_n = \int_{-H_b}^0 \psi_{w,n}(z)\psi_{v,1n}(z)dz + \int_{-h}^{-H_b} \psi_{w,n}(z)\psi_{v,2n}(z)dz$.

Proceeding in a similar manner, using ϕ_{2j} and ϕ_3 from Eqs. 20(b)-(c) in conditions 19(b) near the interface at $x = L_s$, and using the orthogonality of $\psi_{w,m}(z)$, yield

$$T_n e^{ik_{w,n}L_s} a_n - \sum_{n=I,II,0}^{\infty} (A_n e^{-ik_{v,n}L_s} + B_n e^{ik_{v,n}L_s}) b_n = 0, \quad (26a)$$

$$T_n e^{ik_{w,n}L_s} k_{w,n} a_n + \sum_{n=I,II,0}^{\infty} (A_n e^{-ik_{v,n}L_s} - B_n e^{ik_{v,n}L_s}) k_{v,n} b_n = 0, \quad (26b)$$

For computational purpose, the infinite series in Eqs. (25)-(26) are truncated after $n = N$ which together with Eq. (18) give the following $4(N + 1) + 4$ equations:

$$P\vec{x} = \vec{r}, \quad (27)$$

where $\vec{r} = \{R_n, A_n, B_n, T_n\}$ is an unknown column vector to be computed.

Eq. (27) is solved using MATLAB to investigate the effects of wave and sheet parameters on the wave reflection and transmission as well as the displacement of the submerged sheet. Since the analytical analysis is based on the linear wave theory, we only carry out the numerical computation with the submergence $H_s = 0.1 \text{ m}$ which wave breaking is minimal, together with $h = 0.3 \text{ m}$, $T = 0.6 \text{ s}$, $\vartheta = 0.5$, $d_s = 0.01 \text{ m}$, and $L_s = 1.0 \text{ m}$. $\rho = 1025 \text{ kg m}^{-3}$ and $g = 9.81 \text{ m s}^{-2}$ are kept fixed.

The surface displacement of the submerged sheet is calculated using the following formula,

$$\xi(x, t) = i \frac{1}{\omega} \frac{\partial \Phi_{22}}{\partial z} \Big|_{z=-H_s} \quad (28)$$

Fig. 12 shows the comparison between the experimental measurements and analytical predictions for the sheet displacement at two different time instances, only the real values of η and ξ are considered in the plots to represent surface wave and sheet displacement respectively. From the figure, the predictions can capture the locations of crest and trough of both the surface wave and sheet displacement, but the displacement amplitudes are lower. In other words, the analysis resolves the modal shape of the wave-sheet interactions correctly. The larger displacement of submerged sheets in the experiments can be attributed to the small yielding of the stopper rods at the leading and trailing edges due to wave action, as compared to the fixed end condition in the analysis. As

discussed earlier, the end conditions in the field would depend on the exact anchoring arrangement, and small yielding will also be expected unless a firm foundation is provided. The analytical analysis is unable to capture this detail at the moment.

The displacement profile of the sheet along the submerged region is also plotted in Fig. 13a for the three rheological properties. For $T = 0.6$ s, multiple peaks with different amplitudes and frequencies can be observed for the more flexible sheets. With increasing stiffness from $m_{CA} = 4$ to 10%, there is a gradual smoothing with a reduction in displacement amplitude. For the longer periods of $T = 0.8$ and 1.0 s, it can be observed that the number of peaks in the displacement profile also diminishes with increasing sheet stiffness, while the dominant peak amplitude increases at the same time. The above results show that the displacement profile clearly depends on the rheological properties of the sheets.

With the general formulation of the analytical analysis, we can examine the significance of the sheet viscosity independently by comparing the viscoelastic with purely elastic behavior. In Fig. 13b, the shear modulus / elasticity of the three sheets is maintained while the viscosity value is set to zero for comparison. There are no obvious change in the displacement profile for most cases, but significant variations occur in some combinations of wave and sheet characteristics. For $T = 0.8$ s and $m_{CA} = 7\%$, a change in both the phase and amplitude of the displacement profile can be observed. For $T = 0.6$ s and $m_{CA} = 4\%$, the sheet displacement is smoothed, while the opposite occurs for $T = 0.8$ s and $m_{CA} = 10\%$. The comparison thus highlights the need of the viscoelastic model to accurately represent the wave-sheet interactions, the actual behavior of which depends on the field wave conditions and prototype sheet properties.

The effect of sheet thickness on its displacement profile is shown in Fig. 14a based on the analytical analysis. For the more flexible sheets with $m_{CA} = 4$ and 7% and $T = 0.6$ s, the amplitude of sheet displacement initially increases with sheet thickness from $d_s = 0.005$ m to 0.01 m but further increase to $d_s = 0.02$ m reverses the trend, which can be attributed to the complex role of sheet stiffness. In contrast, for the stiffest sheet with $m_{CA} = 10\%$, the decrease in the displacement amplitude with increase in thickness is monotonic. The zero-viscosity comparison is also considered for different sheet thicknesses as shown in Fig. 14b. More notable changes can be observed for the flexible sheets ($m_{CA} = 4\%$ and $d_s = 0.005$ m to 0.01 m), implying that the viscosity plays a bigger role in thinner sheets.

The displacement profile of the submerged sheet with varying sheet length is shown in Fig. 15. Generally, the number of peaks and troughs increases with longer lengths. It is important to note

that the dispersion relation for the submerged sheet should be independent of sheet length, hence the wave number in the region should be the same for different L_s . Here, it can be observed that the location of crests and troughs for different sheet lengths are nearly identical as expected, with only a slight shift which can be attributed to the phase shift of the reflected wave as the length of the submerged sheet changes. In Fig. 16, the displacement profile of the submerged sheet is plotted for different submergences. With increasing submergence, the amplitude of sheet displacement, particularly the dominant peak, decreases as expected due to the decreasing wave action. For flexible sheets with $m_{CA} = 4$ and 7%, multiple wavelengths are clearly visible in the displacement profile when the sheet is held closer to the free surface.

The surface wavenumber along the submerged sheet region has been determined from the experimental measurements as discussed earlier in Section 4. The analytical predictions show a good comparison with the experimental results in general for the flexible sheet with $m_{CA} = 4\%$ (Fig. 7). When the stiffness increases to $m_{CA} = 7\%$, the predictions for the dispersion relation with longer waves follow the open water condition with $h = 0.3$ m, but the experimental results show wave shortening instead, implying a notable discrepancy here. With further increase in sheet stiffness to $m_{CA} = 10\%$, for the longer waves, the predictions remain following the open water wavenumber with $h = 0.3$ m, while the experimental results show the wave number with $h = 0.1$ m instead. The dominant wave number k_v^+ for viscoelastic plate covered region S_{22} , increases with the increase of plate stiffness. This lengthening of flexural wave for higher stiffness plate can be observed in Fig. 16. Overall, the theory is not able to capture well the variation in wavenumber with submergence for longer waves with stiff submerged sheets. Large discrepancy is also observed between the experimental results and analytical prediction for the reflection coefficient as shown in Fig. 9, with the experimental results up to five times larger. This discrepancy can probably be contributed to the difference in the end conditions for the submerged sheets again as discussed above.

6. Conclusions

A novel experimental study is carried to examine the surface wave interactions with submerged viscoelastic sheets of varying rheological properties using oil-doped PDMS. The experimental results show that the wave-sheet interactions are complex. With the deeper submergence $H_s = 0.1$ m, the wave pattern in the submerged sheet region depends significantly on the rheological properties of the sheet. When the submergence is reduced to $H_s = 0.075$ m, a standing wave pattern with primarily lower order modes develops along the flexible sheet ($m_{CA} = 4\%$) with a significant reduction of transmitted wave energy past the sheet region for shorter period

waves. The standing wave pattern diminishes with further increase in the wave period to 0.9 to 1.0s. With the smallest submergence $H_s = 0.05$ m, a significant reduction in wave energy transmission occurs for all combinations of waver periods and sheet characteristics. In fact, an almost complete cutoff (up to 99% reduction in wave energy transmission) with the flexible sheet $m_{CA} = 4\%$ held close to the mean water level (MWL). For the other two stiffer sheets with $m_{CA} = 7\%$ and 10% , 50-90% reduction in wave energy transmission is recorded when the sheet is held close to the MWL.

A theoretical analysis is also performed based on the linear wave theory with the viscoelastic representation of the Voigt model. The analysis enables the examination of the different parameters, and in particular the role of viscosity in the viscoelastic representation of the sheet characteristics. Comparing to the measurements, the locations of crest and trough of surface wave displacement as well as sheet displacement are well predicted. However, the displacement amplitude is typically underestimated due to the fixed end conditions assumed as well as the Euler-Bernoulli beam approach for the analysis. In addition, the predicted dispersion relation for the surface waves agrees well with the experimental results for the shorter period waves, however larger discrepancies are observed for the longer period waves, with the experimental results showing wave lengthening with stiff submerged viscoelastic sheets while the analysis predicts the opposite. It is however unclear at this point whether the difference is also attributable to the end conditions. Thus, further analysis incorporating the movable end conditions will need to be developed in the future.

Finally, the current analysis is performed under the assumption of Stokes linear wave theory. However, from the wave damping results showing in Table 4 for the various submergences and viscoelastic properties in the experiments, the waves on top of the viscoelastic sheet would reach a high wave steepness that would require the analysis for the wave nonlinearity reaching the Stokes 3rd order. Further improvement in the analysis using higher order wave theory will also be necessary in the future.

Acknowledgement

This research study is funded by the internal core funding from the Nanyang Environment and Water Research Institute (NEWRI), Nanyang Technological university.

References:

1. Buriani, F. and Renzi, E., 2017. Hydrodynamics of a flexible piezoelectric wave energy harvester moored on a breakwater. 12th European Wave and Tidal Energy Conference (EWTEC) Cork, Ireland.
2. Burke, J.E., 1964. Scattering of surface waves on an infinitely deep fluid. *J. Math. Phys.*, 5 (6), pp.805-819.
3. Cho, I.H. and Kim, M.H., 1998. Interactions of a horizontal flexible membrane with oblique incident waves. *Journal of Fluid Mechanics*, 367, pp.139-161.
4. Cho, I.H. and Kim, M.H., 1999. Wave deformation by a submerged flexible circular disk. *Applied ocean research*, 21(5), pp.263-280.
5. Cho, I.H. and Kim, M.H., 2000. Interactions of horizontal porous flexible membrane with waves. *Journal of waterway, port, coastal, and ocean engineering*, 126(5), pp.245-253.
6. Cho, I.H., Koh, H.J., Kim, J.R. and Kim, M.H., 2013. Wave scattering by dual submerged horizontal porous plates. *Ocean engineering*, 73, pp.149-158.
7. Dai, J., Wang, C.M., Utsunomiya, T. and Duan, W., 2018. Review of recent research and developments on floating breakwaters. *Ocean Engineering*, 158, pp.132-151.
8. Fang, Z., Xiao, L., Kou, Y. and Li, J., 2018. Experimental study of the wave-dissipating performance of a four-layer horizontal porous-plate breakwater. *Ocean Engineering*, 151, pp.222-233.
9. Fox, C. and Squire, V.A., 1994. On the oblique reflexion and transmission of ocean waves at shore fast sea ice, *Philos. TR Soc. A.*, 347, pp.185–218.
10. Greene, T. R., and Heins, A. E., 1953. Water waves over a channel of infinite depth, *Quarterly of Applied Mathematics*, Vol. 11, No. 2, pp.201-214.
11. Hassan, M.U., Meylan, M.H. and Peter, M.A., 2009. Water-wave scattering by submerged elastic plates. *The Quarterly Journal of Mechanics & Applied Mathematics*, 62(3), pp.321-344.
12. He, F., Huang, Z. and Law, A.W.K., 2012. Hydrodynamic performance of a rectangular floating breakwater with and without pneumatic chambers: An experimental study. *Ocean Engineering*, 51, pp.16-27.
13. He, F., Huang, Z. and Law, A.W.K., 2013. An experimental study of a floating breakwater with asymmetric pneumatic chambers for wave energy extraction. *Applied energy*, 106, pp.222-231.

14. Heins, A. E., 1950. Water waves over a channel of finite depth with a submerged plane barrier, *Canadian Journal of Mathematics*, Vol. 2, pp.210- 222.
15. Huang, G. and Law, A.W.K., 2013. Wave-induced drift of large floating objects in regular waves. *Journal of Waterway Port Coastal and Ocean Engineering*, ASCE, 139(6), pp.535-542.
16. Kee, S.T. and Kim, M.H., 1997. Flexible membrane wave barrier. II: floating/submerged buoy-membrane system. *Journal of waterway, port, coastal, and ocean engineering*, 123(2), pp.82-90.
17. Kim, M.H. and Kee, S.T., 1996. Flexible-membrane wave barrier. I: Analytic and numerical solutions. *Journal of waterway, port, coastal, and ocean engineering*, 122(1), pp.46-53.
18. Law, A.W.K., 1999. Wave-induced surface drift of an inextensible thin film. *Ocean Engineering*, 26(11), pp.1145-1168.
19. Liu, Y. and Li, H.J., 2014. Wave scattering by dual submerged horizontal porous plates: Further results. *Ocean engineering*, 81, pp.158-163.
20. Mohapatra, S.C., Sahoo, T. and Soares, C.G., 2018a. Interaction between surface gravity wave and submerged horizontal flexible structures. *Journal of Hydrodynamics*, 30(3), pp.481-498.
21. Mohapatra, S.C., Sahoo, T. and Soares, C.G., 2018b. Surface gravity wave interaction with a submerged horizontal flexible porous plate. *Applied Ocean Research*, 78, pp.61-74.
22. Mosig, J.E., Montiel, F. and Squire, V.A., 2015. Comparison of viscoelastic-type models for ocean wave attenuation in ice-covered seas. *Journal of Geophysical Research: Oceans*, 120(9), pp.6072-6090
23. Neelamani, S. and Reddy, M.S., 1992. Wave transmission and reflection characteristics of a rigid surface and submerged horizontal plate. *Ocean engineering*, 19(4), pp.327-341.
24. Ohkusu, M. and Namba, Y., 2004. Hydroelastic analysis of a large floating structure. *Journal of Fluids and Structures*, 19(4), pp.543-555.
25. Patarapanich, M., 1984. Maximum and zero reflection from submerged plate. *Journal of waterway, port, coastal, and ocean engineering*, 110(2), pp.171-181.
26. Patarapanich, M. and Cheong, H.F., 1989. Reflection and transmission characteristics of regular and random waves from a submerged horizontal plate. *Coastal engineering*, 13(2), pp.161-182.
27. Popov, V.L., He, M., and Willert, E., 2019. Viscoelastic Materials. *Handbook of Contact Mechanics*, pp.213-249.

28. Renzi, E., 2016. Hydroelectromechanical modelling of a piezoelectric wave energy converter. *Proceedings of the Royal Society A: Mathematical, Physical and Engineering Sciences*, 472(2195), pp.20160715.
29. Shugan, I.V., Hwung, H.H., Yang, R.Y. and Hsu, W.Y., 2012. Elastic plate as floating wave breaker in a beach zone. *Physics of Wave Phenomena*, 20(3), pp.199-203.
30. Siew, P. F., and Hurley, D. G., 1977. Long surface waves incident on a submerged horizontal plate, *Journal of Fluid Mechanics*, Vol. 83, Part 1, pp.141-151.
31. Sree, D.K., Law, A.W.K. and Shen, H.H., 2017. An experimental study on the interactions between surface waves and floating viscoelastic covers. *Wave Motion*, 70, pp.195-208.
32. Sree, D.K., Law, A.W.K. and Shen, H.H., 2018. An experimental study on gravity waves through a floating viscoelastic cover. *Cold Regions Science and Technology*, 155, pp.289-299.
33. Sun, Z., Zhang, N., Law, A.W.K., and Huang, G., 2018. Dynamic loading on flexible floating anti-collision system due to head-on collision by uncontrolled vessel. *Journal of Waterway, Port, Coastal, and Ocean Engineering*, ASCE, 144 (3), 05018001.
34. Williams, T.D. and Meylan, M.H., 2012. The Wiener–Hopf and residue calculus solutions for a submerged semi-infinite elastic plate. *Journal of Engineering Mathematics*, 75(1), pp.81-106.
35. Yang, R.Y., Wu, Y.C. and Hwung, H.H., 2012. Beach erosion management with the application of soft countermeasure in Taiwan. *Sustainable development: Authoritative and leading-edge content for environmental management*, Intechopen publishing, pp.349-370.

List of Symbols

\tilde{E}_{wL}	Normalized wave energy near leading edge
\tilde{E}_{wT}	Normalized wave energy near trailing edge
M_B	Mass of base elastomer
M_{CA}	Mass of curing agent
M_o	Mass of oil
ξ_r	Relaxation time
A_o	Incident wave amplitude
C_r	Reflection coefficient
E_w	Wave energy
G'	Storage modulus
G_v	Complex Voigt shear modulus
H_s	Depth of submergence
L_s	Length of submerged sheet
R_o	Reflected wave amplitude
S_1	Region 1
S_{21}	Region 2
S_{22}	Region 3
S_3	Region 4
T_r	Transmission coefficient
c_p	Phase velocity
d_s	Sheet thickness
k_R	Wavenumber for reflected wave
k_o	Open water wavenumber
m_{CA}	Mass percentage of curing agent
m_o	Mass percentage of oil
m_s	Mass per unit area of sheet
p_s	Pressure acting across the sheet surface
r_e	Percentage of wave energy reduction
ρ_s	Density of sheet
ϕ_R	Phase of reflected wave
ϕ_S	Phase shift

ϕ_j	Spatial velocity potential at the j^{th} region
h	Water depth
H	Wave height
G	Shear modulus
G''	Loss modulus
T	Waveperiod
g	Acceleration due to gravity
k	Wavenumber
t	Time
γ	Shear strain
η	Vertical water surface displacement
λ	Wavelength
μ	Dynamic viscosity
ν	Kinematic viscosity
ξ	Submerged sheet displacement
ρ	Density
τ	Shear stress
ω	Rotational frequency of rheometer/ wave frequency
ϑ	Poisson ratio
ϕ	Phase of the incident wave

List of Abbreviations

PDMS	Polydimethylsiloxane
MWL	Mean Water Level
RGB	Red, Green, and Blue
US	Ultrasound

List of Figures

- Fig. 1: Viscoelastic properties against angular frequency (Curing Period: circles = 1 week; asterisk = 2 weeks; diamond = 3 weeks).
- Fig. 2: Schematic diagram of the experimental setup.
- Fig. 3a: Time series data for $H_s = 0.1$ m ($T = 0.6$ s, $m_{CA} = 7\%$). The boxed portion is used for analysis.
- Fig. 3b: Time series data for $H_s = 0.075$ m ($T = 0.6$ s, $m_{CA} = 7\%$). The boxed portion is used for analysis.
- Fig. 3c: Time series data for $H_s = 0.05$ m ($T = 0.6$ s, $m_{CA} = 7\%$). The boxed portion is used for analysis.
- Fig. 4: Energy spectrum for $T = 0.6$ s and $m_{CA} = 7\%$.
- Fig. 5: Profile of surface wave and submerged viscoelastic sheet at $t =$ (a) 8.73 s and (b) 8.73 s + $\frac{T}{2}$ from the beginning of the experiment ($T = 0.6$ s, $m_{CA} = 7\%$, $H_s = 0.1$ m). Left - grey scale; Right - corresponding digitized data.
- Fig. 6: Digitized profile of surface wave at t and $t + \Delta t$ ($T = 0.6$ s, $m_{CA} = 7\%$, $H_s = 0.1$ m), with the spatial shift Δx that yields the best match.
- Fig. 7: Dispersion relation of surface wave along submerged sheet region ($H_s = 0.1$ m). Experimental data - black markers; Theoretical predictions - grey solid lines. Open water wavenumber: dotted line $h = 0.3$ m, and dash line $h = 0.1$ m.
- Fig. 8: Fitted time series profile for the experiment ($T = 0.6$ s, $m_{CA} = 7\%$, $H_s = 0.1$ m).
- Fig. 9: (a) Reflection coefficient, (b) reflected wavenumber, and (c) transmission coefficient. Experiments: m_{CA} (%): Circles = 4, Asterisk = 7, and Triangle = 10. Predictions: m_{CA} (%): Solid line = 4, Dash-dotted line = 7, and Dotted line = 10.
- Fig. 10a: Grey scale profile of surface wave and sheet displacement for different wave periods and submergences ($m_{CA} = 4\%$). 1V:2.5H scale.
- Fig. 10b: Grey scale profile of surface wave and sheet displacement for different wave periods and submergences ($m_{CA} = 7\%$). 1V:2.5H scale.
- Fig. 10c: Grey scale profile of surface wave and sheet displacement for different wave periods and submergences ($m_{CA} = 10\%$). 1V:2.5H scale.
- Fig. 11: Schematic diagram for the analysis.
- Fig. 12: Comparison of profile between surface wave and submerged sheet profile with experimental data ($T = 0.6$ s, $m_{CA} = 7\%$, and $H_s = 0.1$ m). Profile at (a) $t = 8.73$ s, and (b) $t = 8.73$ s + $\frac{T}{2}$ from the beginning of the experiment.

Fig. 13a: Predictions of sheet displacement profile (finite viscosity) at $t = T$. m_{CA} (%): solid line = 4, dash-dot line = 7, and dotted line = 10. T (s): (a) 0.6, (b) 0.8 and (c) 1.0.

Fig. 13b: Predictions of sheet displacement profile (zero viscosity) at $t = T$. m_{CA} (%): solid line = 4, dash-dot line = 7, and dotted line = 10. T (s): (a) 0.6, (b) 0.8 and (c) 1.0.

Fig. 14a: Sheet displacement profile with different thickness (finite viscosity) at $t = T = 0.6$ s. m_{CA} (%): (a) 4, (b) 7, and (c) 10. d_s ($\times 10^{-2}$ m): grey solid line = 0.5, black solid line = 1.0 and black dotted line = 2.0.

Fig. 14b: Sheet displacement profile with different thickness (zero viscosity) at $t = T = 0.6$ s. m_{CA} (%): (a) 4, (b) 7, and (c) 10. d_s ($\times 10^{-2}$ m): grey solid line = 0.5, black solid line = 1.0 and black dotted line = 2.0.

Fig. 15: Sheet displacement profile with different length ($m_{CA}=7\%$, $d_s = 0.01$ m, $H_s = 0.1$ m) at $t = T = 0.6$ s. L_s (m): black solid line = 1.0, dotted line = 2.5, and grey solid line = 5.0.

Fig. 16: Sheet displacement profile with different submergences, $d_s = 0.01$ m at $t = T = 0.6$ s. m_{CA} (%): solid line = 4, dash-dot line = 7, and dotted line = 10.

List of Tables

Table 1: Shear modulus and viscosity of oil-doped PDMS sheets based on Voigt model

Table 2: Input wave characteristics.

Table 3: Wave energy reduction for open water case.

Table 4: Wave energy reduction due to submerged viscoelastic sheet.

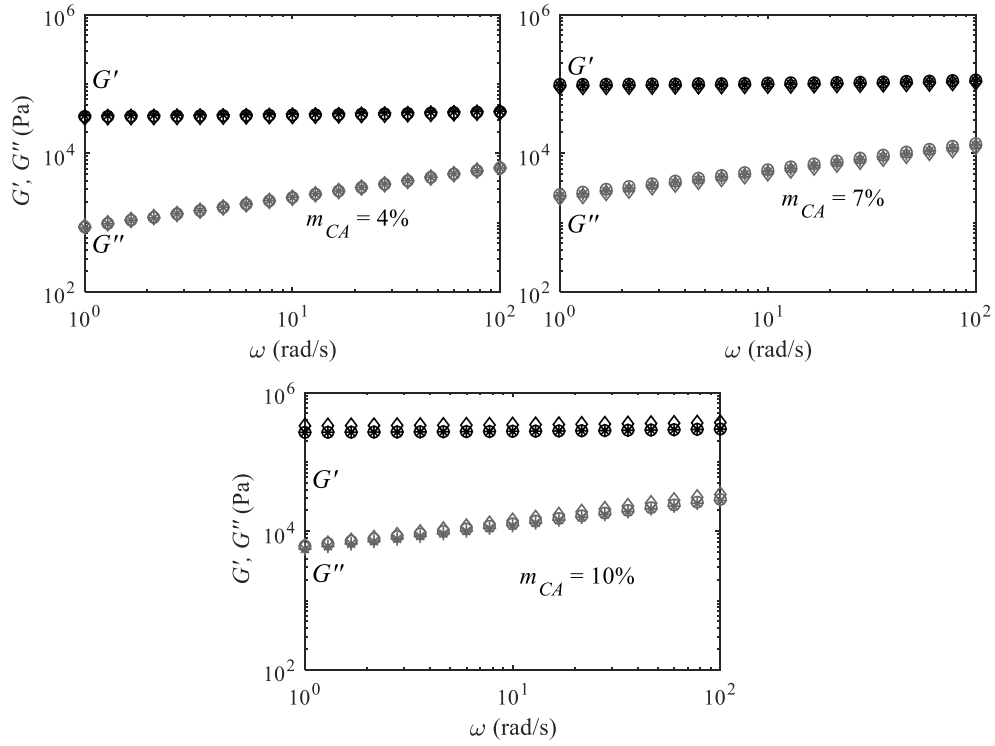


Fig. 1: Viscoelastic properties against angular frequency (Curing Period: circles = 1 week; asterisk = 2 weeks; diamond = 3 weeks).

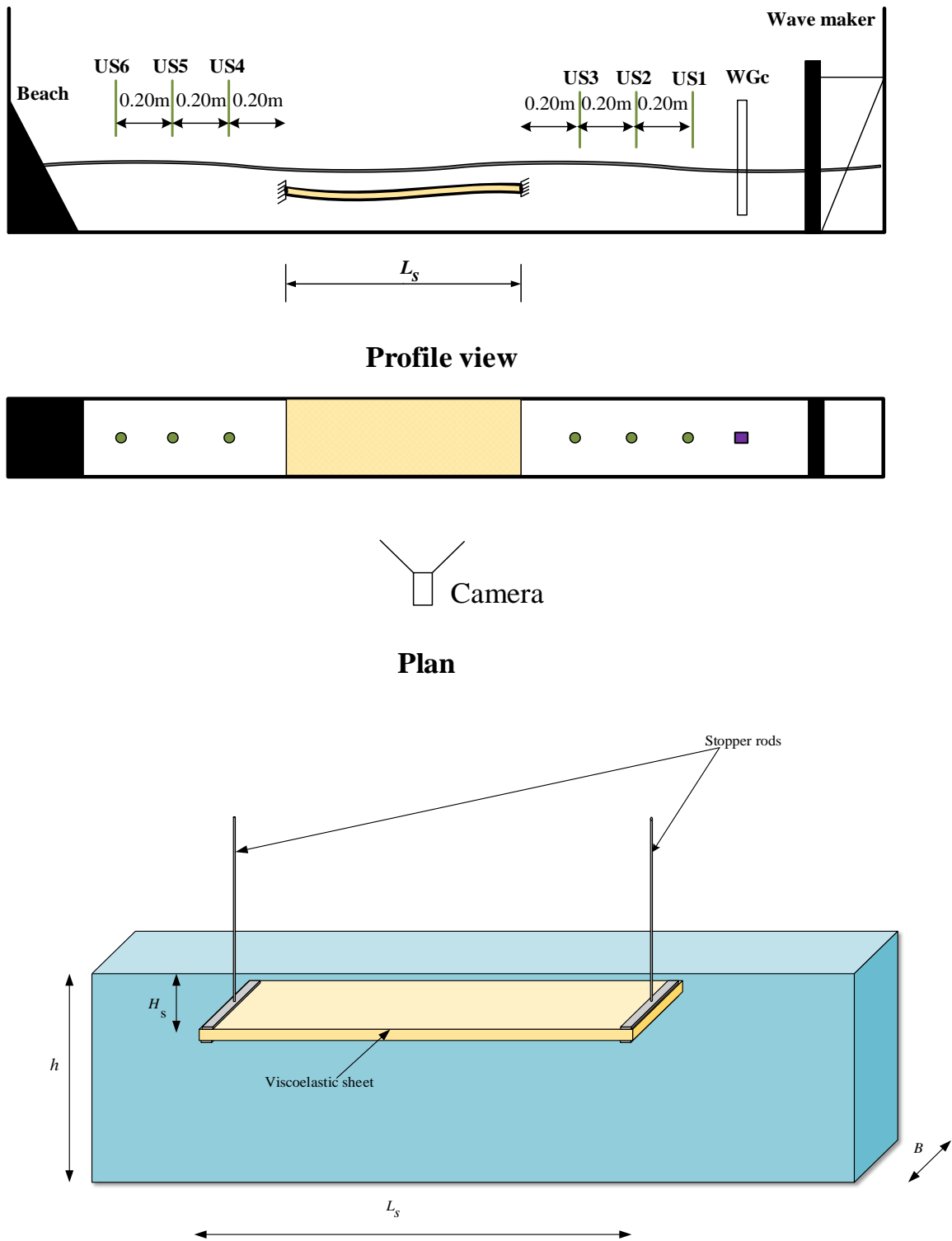


Fig. 2: Schematic diagram of the experimental setup.

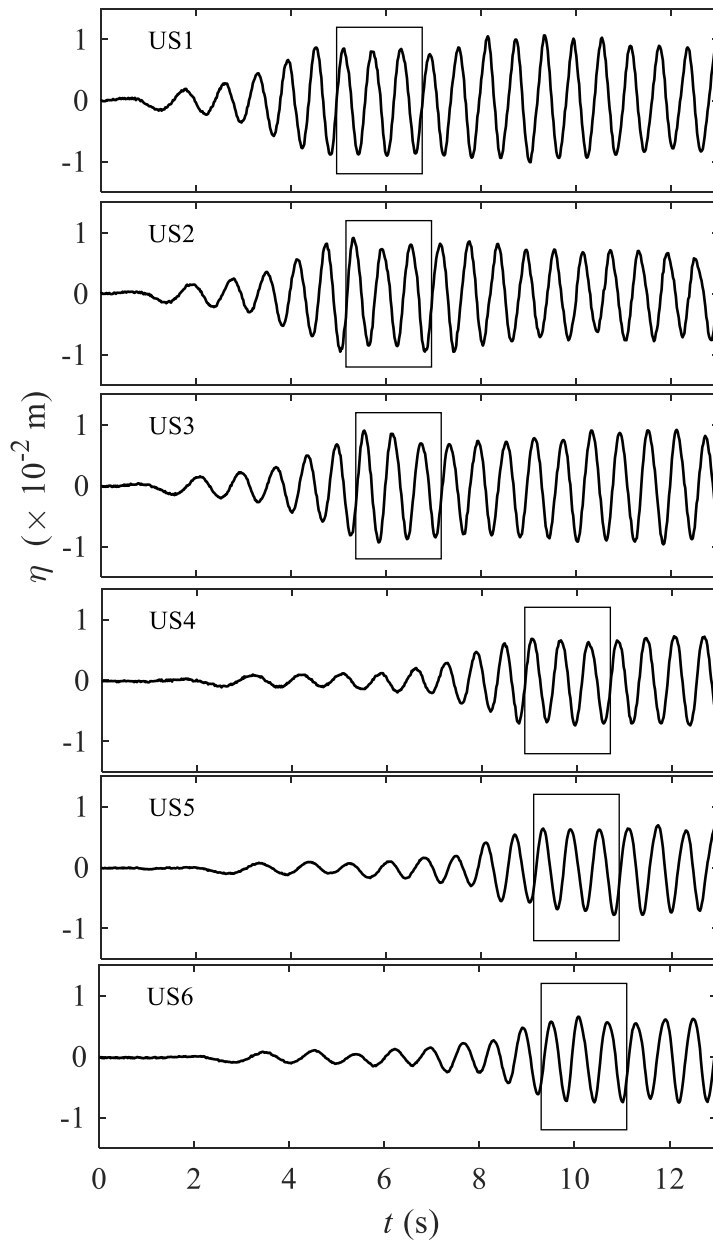


Fig. 3a: Time series data for $H_s = 0.1$ m ($T = 0.6$ s, $m_{CA} = 7\%$). The boxed portion is used for analysis.

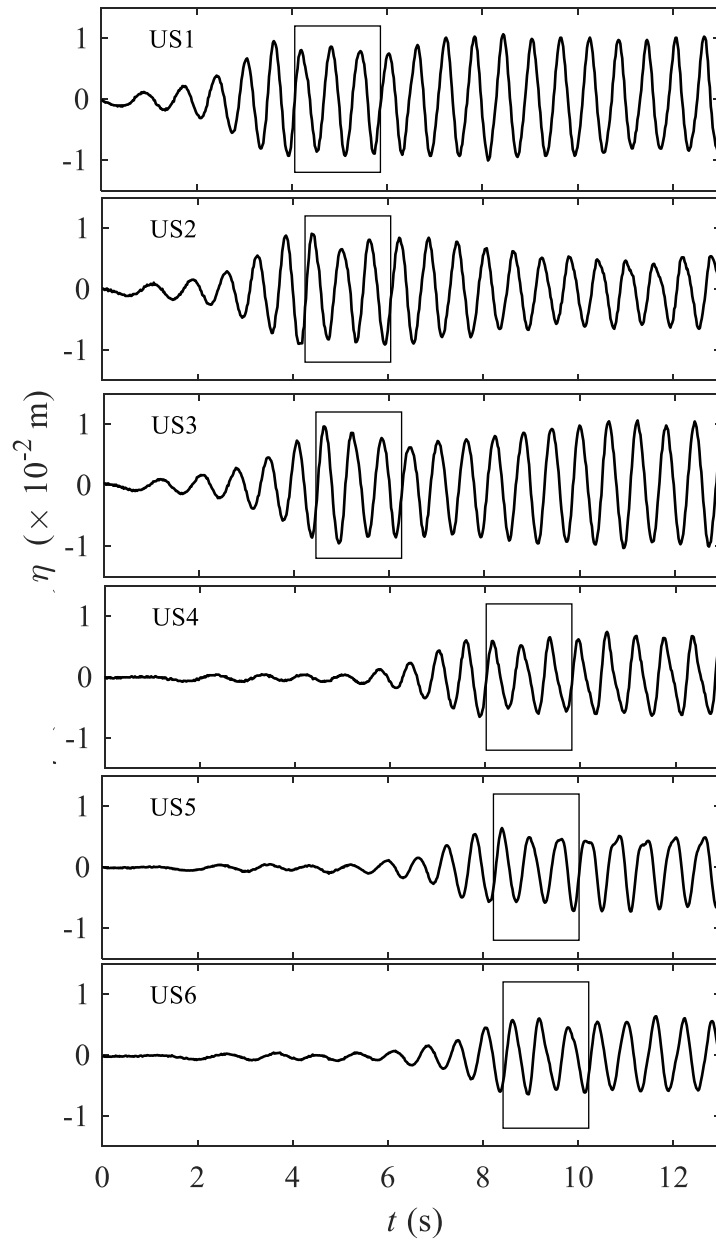


Fig. 3b: Time series data for $H_s = 0.075$ m ($T = 0.6$ s, $m_{CA} = 7\%$). The boxed portion is used for analysis.

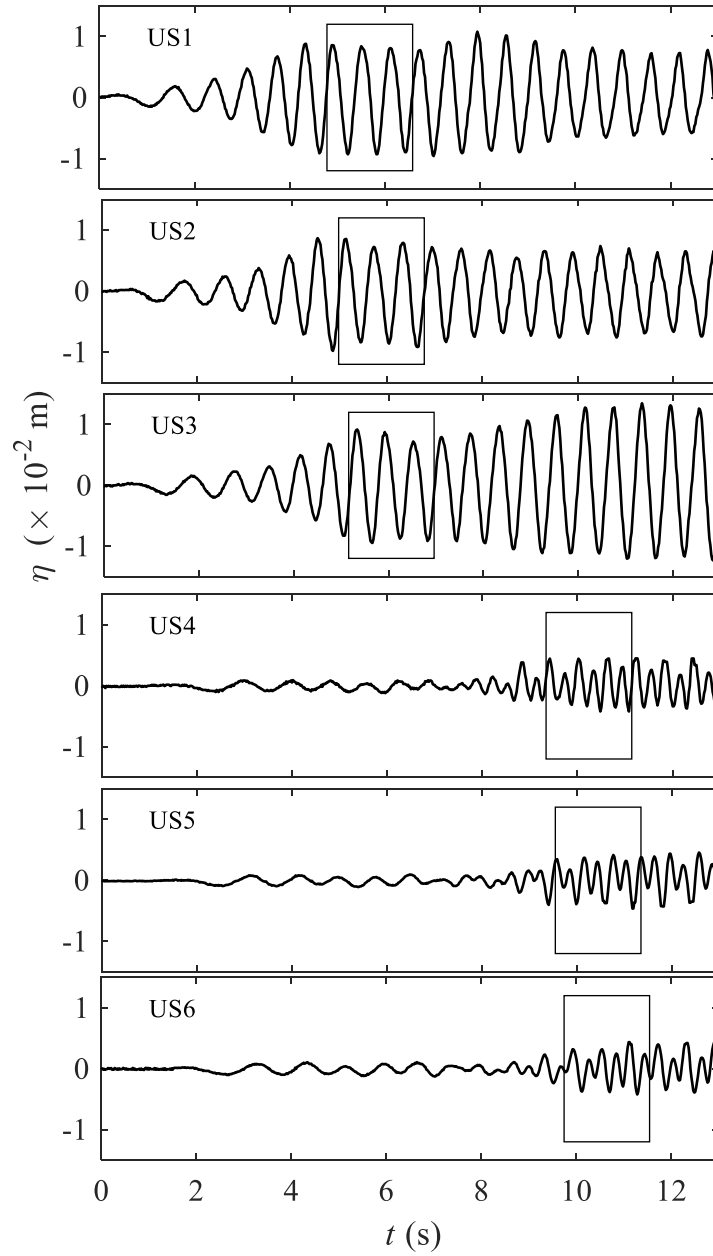


Fig. 3c: Time series data for $H_5 = 0.05$ m ($T = 0.6$ s, $m_{CA} = 7\%$). The boxed portion is used for analysis.

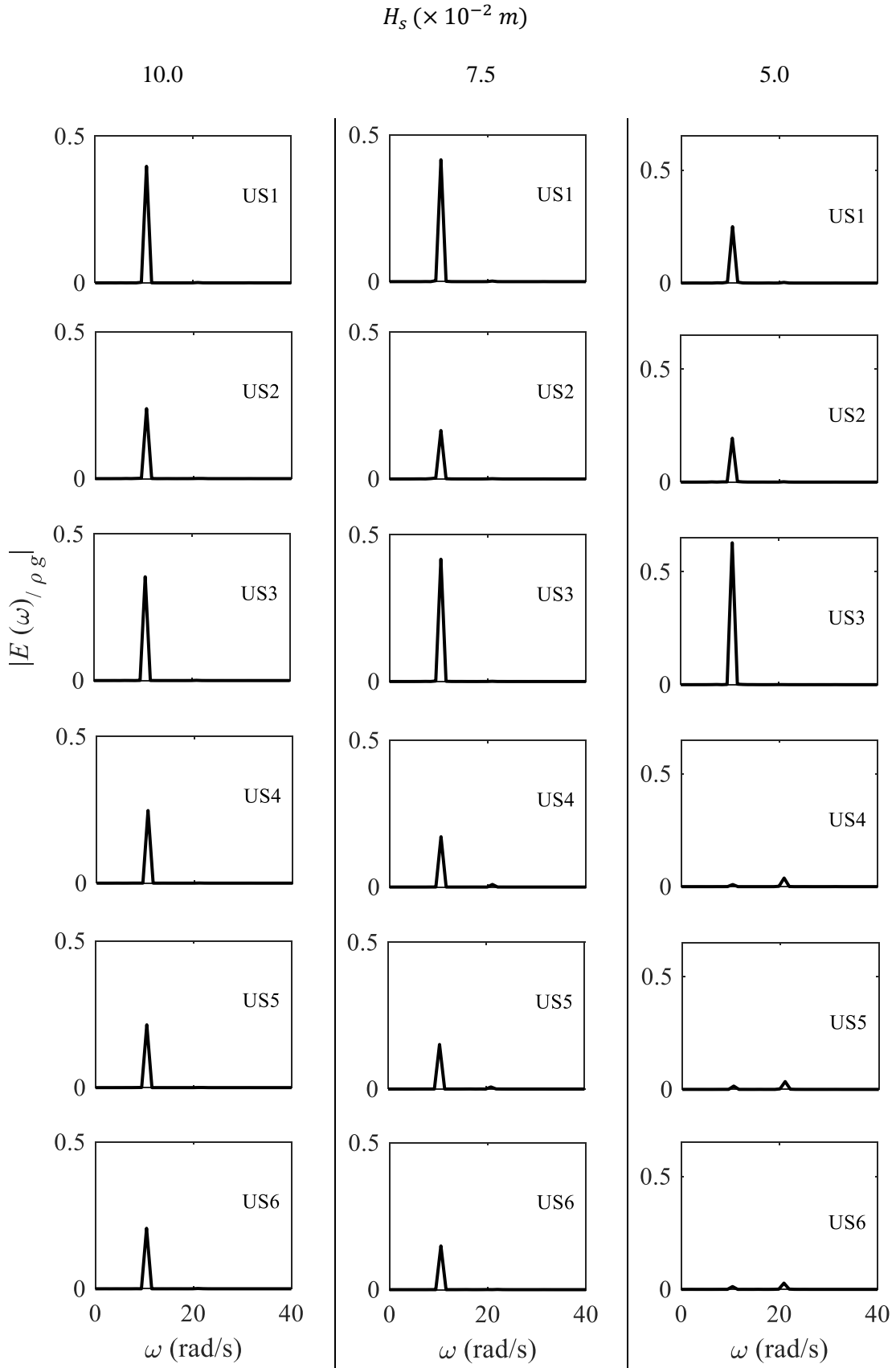


Fig. 4: Energy spectrum for $T = 0.6$ s and $m_{CA} = 7\%$.

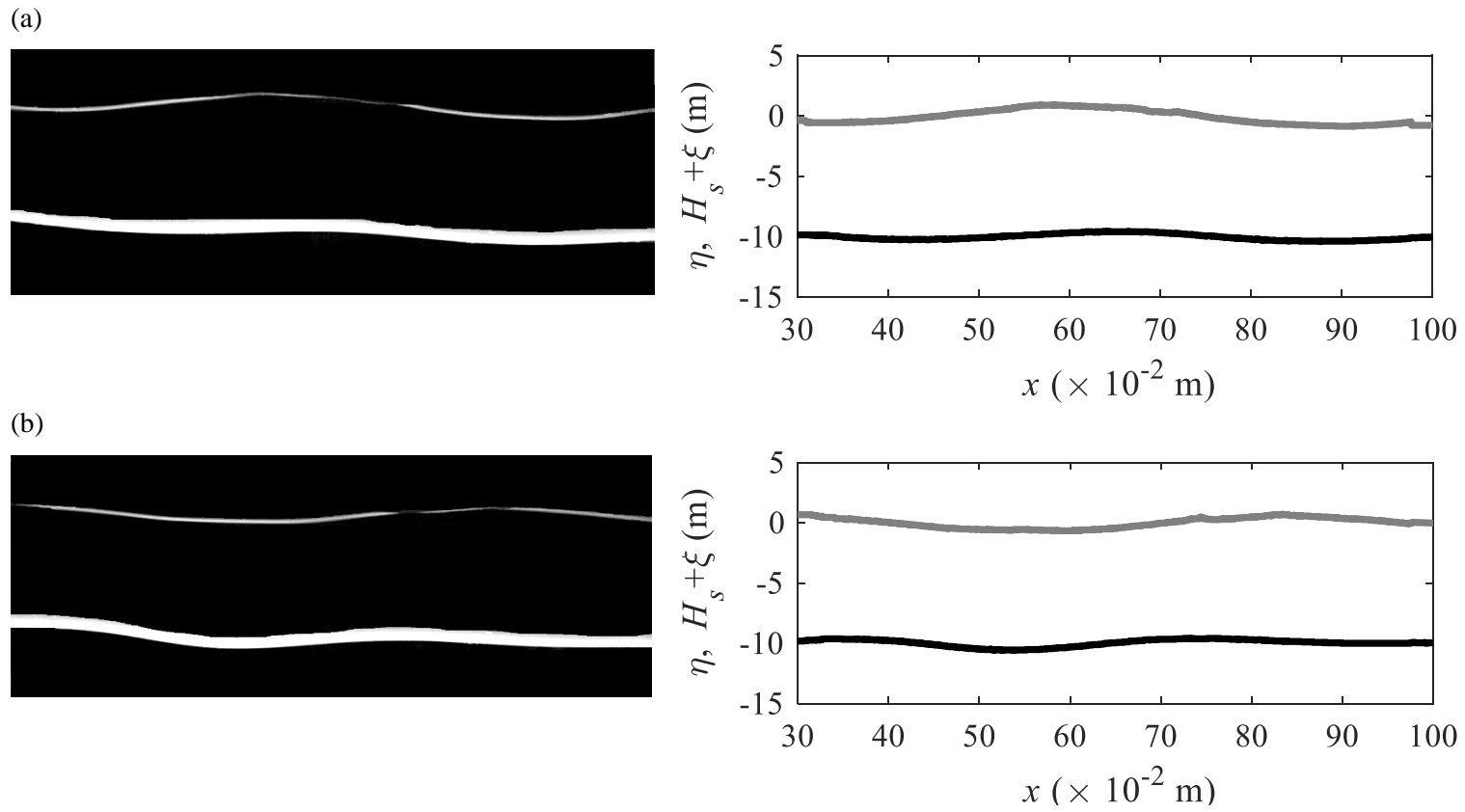


Fig. 5: Profile of surface wave and submerged viscoelastic sheet at $t =$ (a) 8.73 s and (b) $8.73 \text{ s} + \frac{T}{2}$ from the beginning of the experiment ($T = 0.6 \text{ s}$, $m_{CA} = 7\%$, $H_s = 0.1 \text{ m}$). Left - grey scale; Right - corresponding digitized data.

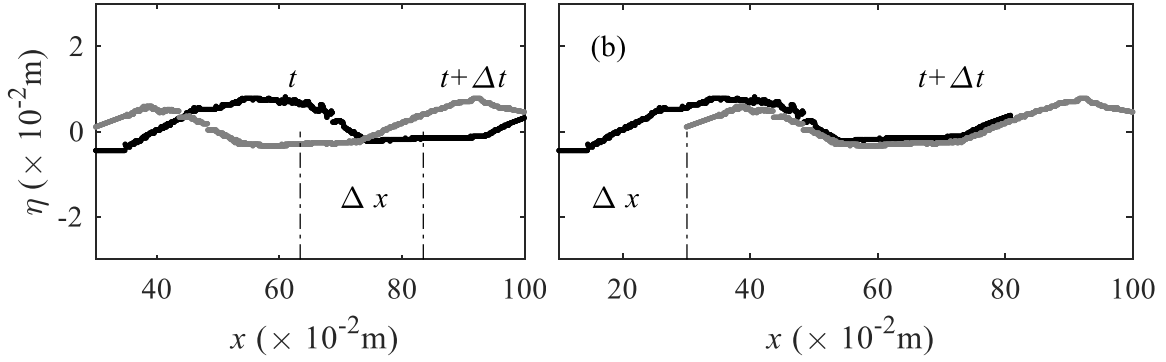


Fig. 6: Digitized profile of surface wave at t and $t + \Delta t$ ($T = 0.6$ s, $m_{CA} = 7\%$, $H_s = 0.1$ m), with the spatial shift Δx that yields the best match.

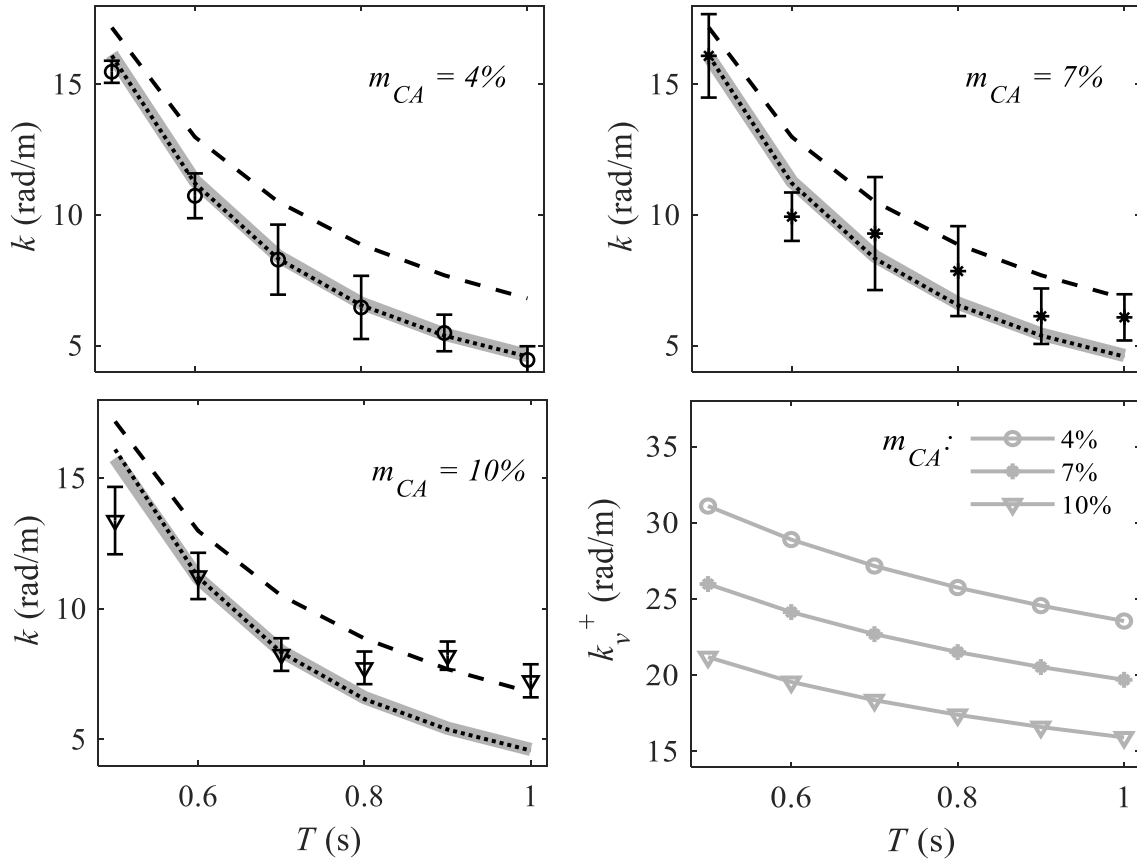


Fig. 7: Dispersion relation of surface wave along submerged sheet region ($H_s = 0.1$ m). Experimental data - black markers; Theoretical predictions - grey solid lines. Open water wavenumber: dotted line $h = 0.3$ m, and dash line $h = 0.1$ m.

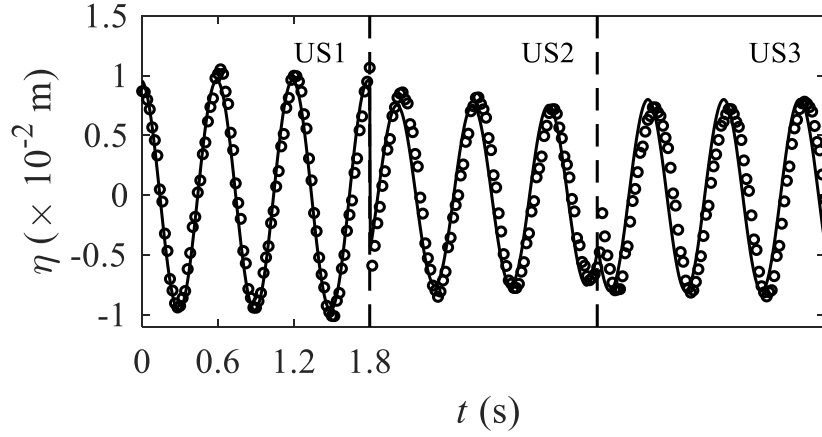


Fig. 8: Fitted time series profile for the experiment ($T = 0.6$ s, $m_{CA} = 7\%$, $H_s = 0.1$ m).

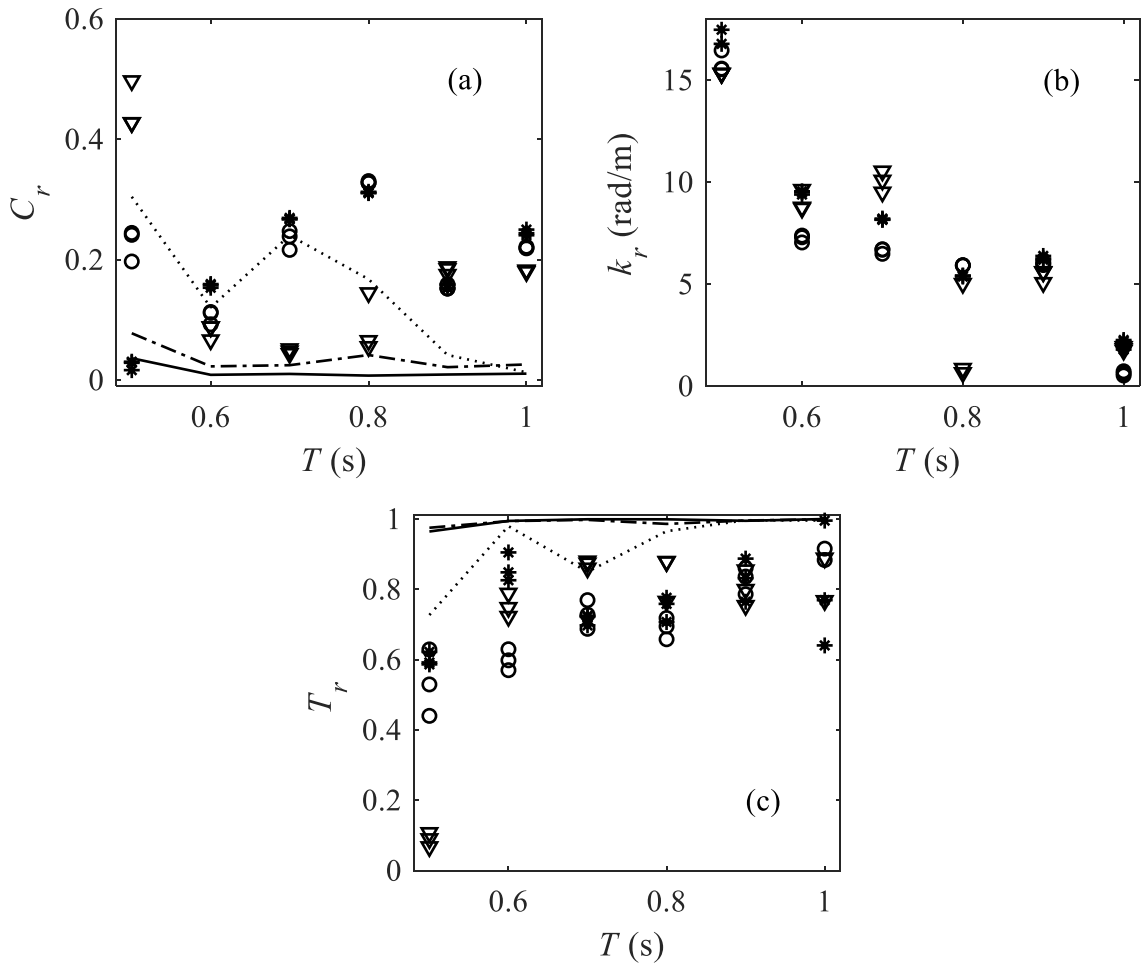


Fig. 9: (a) Reflection coefficient, (b) reflected wavenumber, and (c) transmission coefficient.

Experiments: m_{CA} (%): Circles = 4, Asterisk = 7, and Triangle = 10. Predictions: m_{CA} (%):

Solid line = 4, Dash-dotted line = 7, and Dotted line = 10.

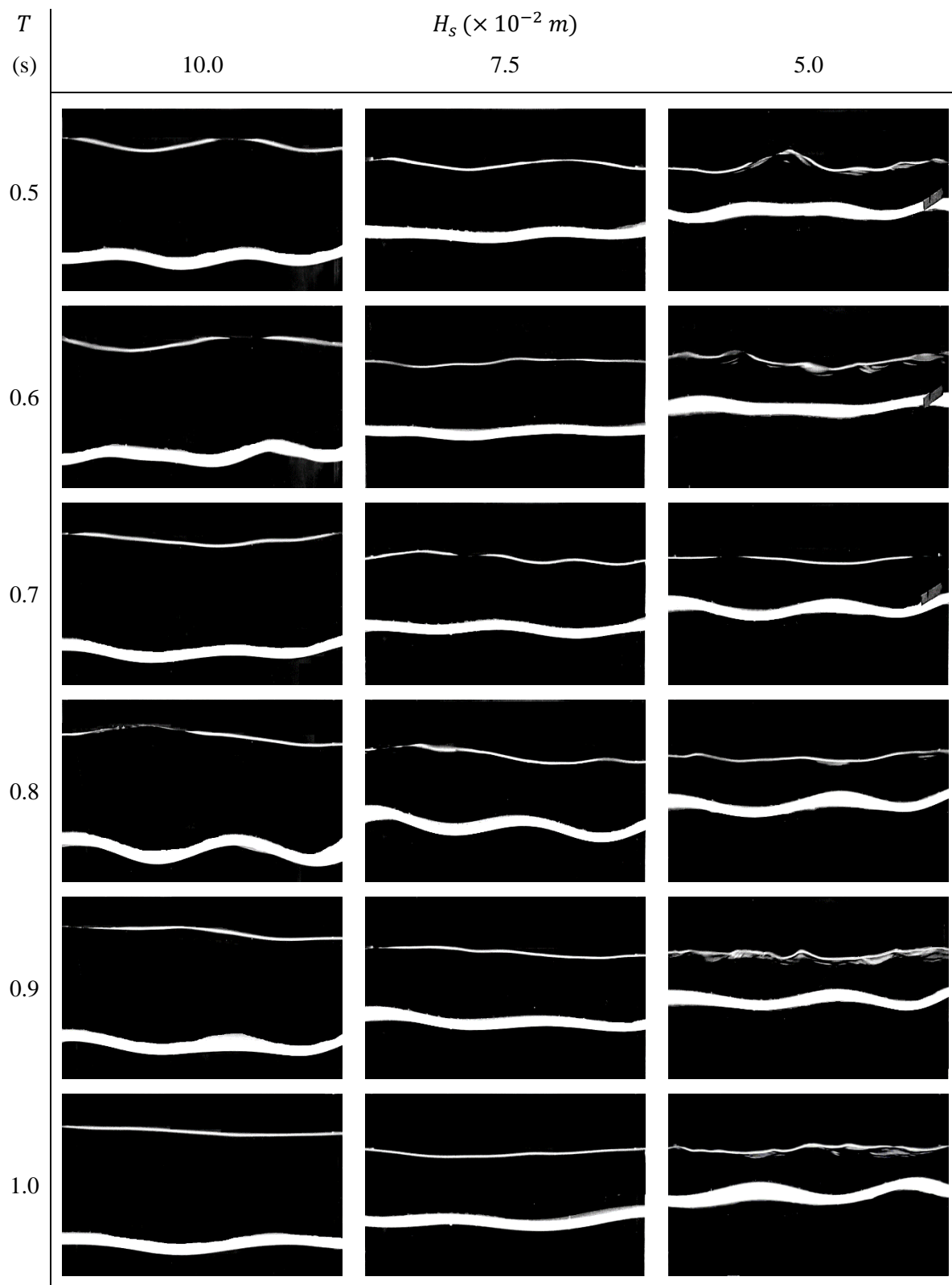


Fig. 10a: Grey scale profile of surface wave and sheet displacement for different wave periods and submergences ($m_{CA} = 4\%$). 1V:2.5H scale.

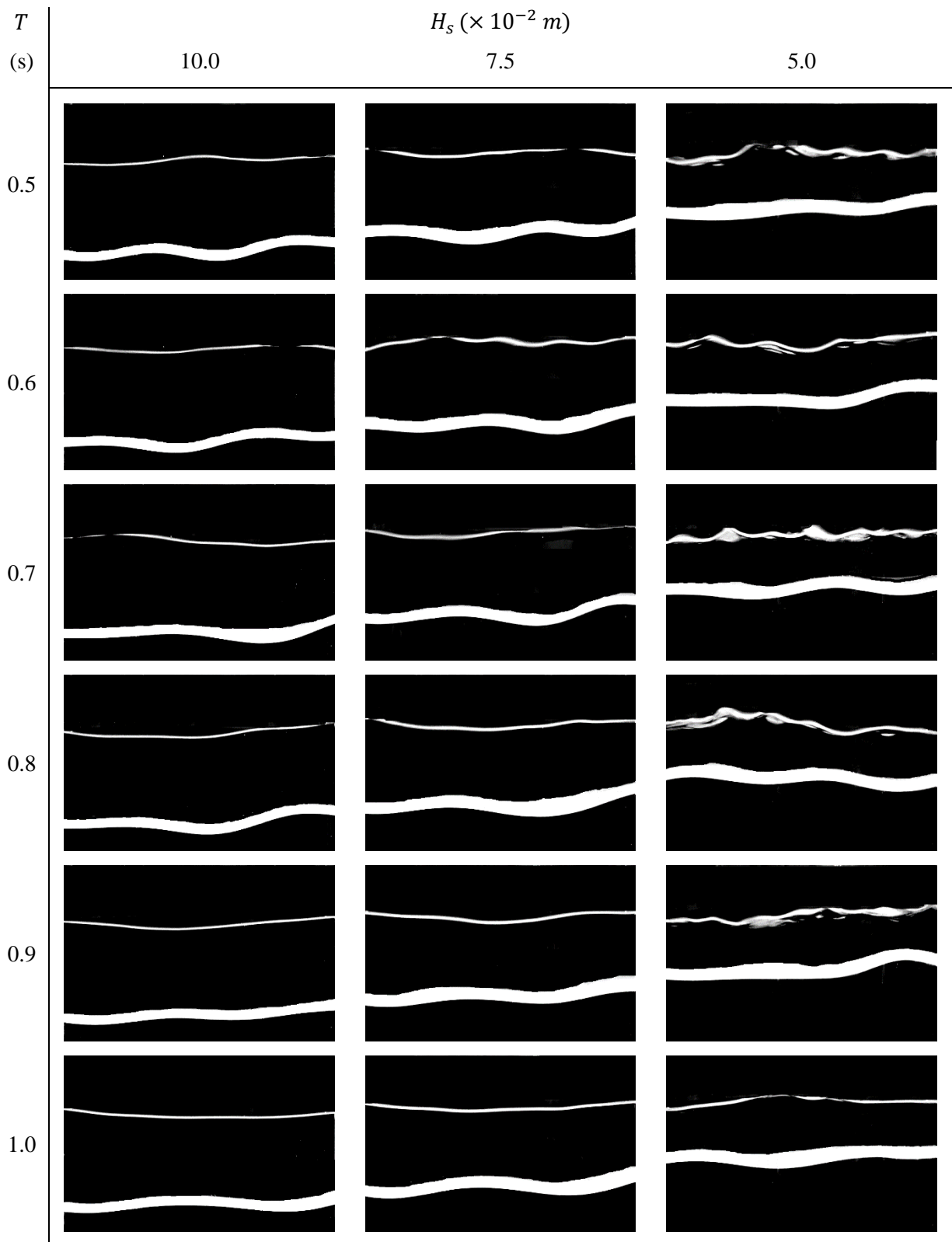


Fig. 10b: Grey scale profile of surface wave and sheet displacement for different wave periods and submergences ($m_{CA} = 7\%$). 1V:2.5H scale.

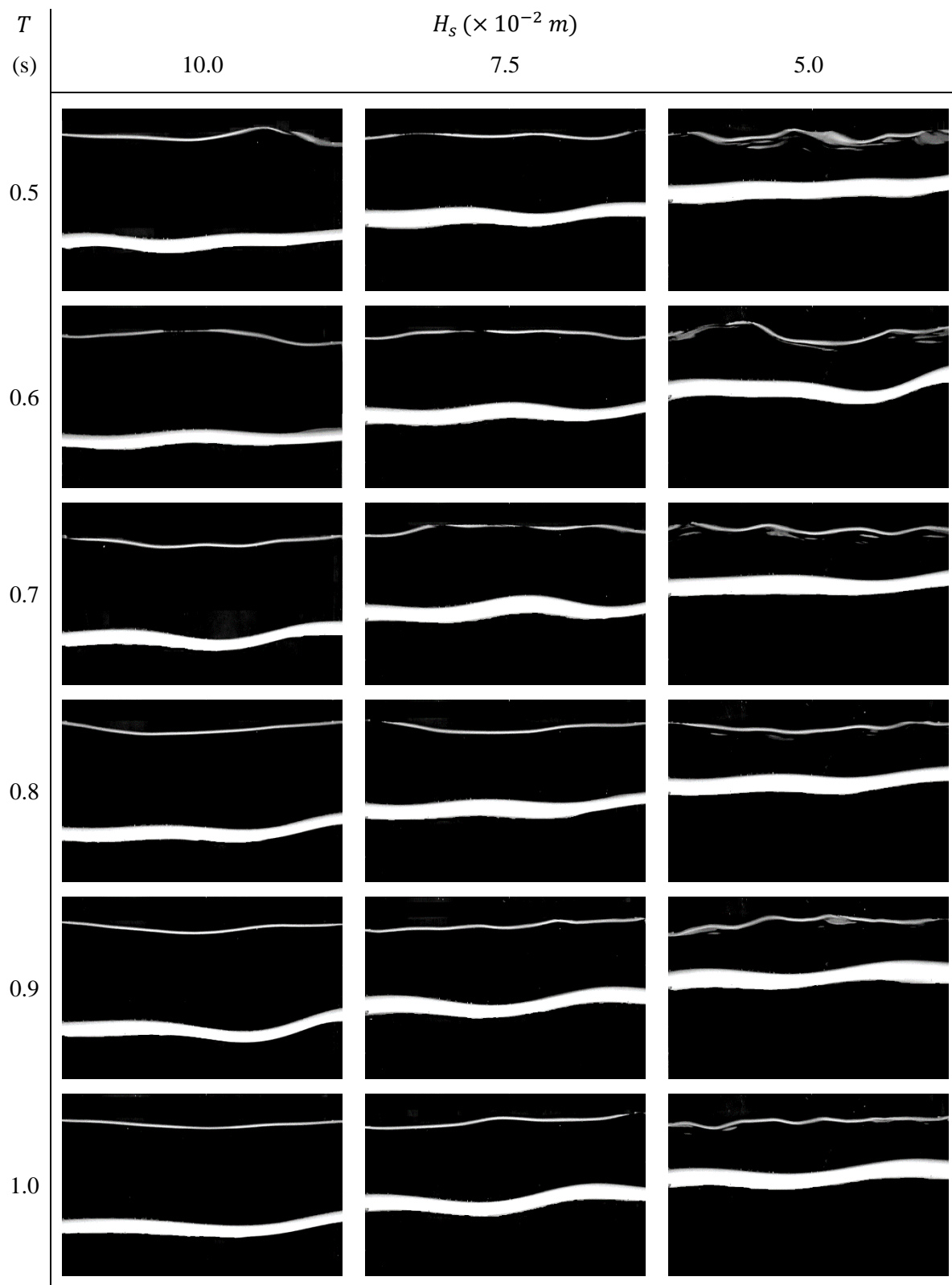


Fig. 10c: Grey scale profile of surface wave and sheet displacement for different wave periods and submergences ($m_{CA} = 10\%$). 1V:2.5H scale.

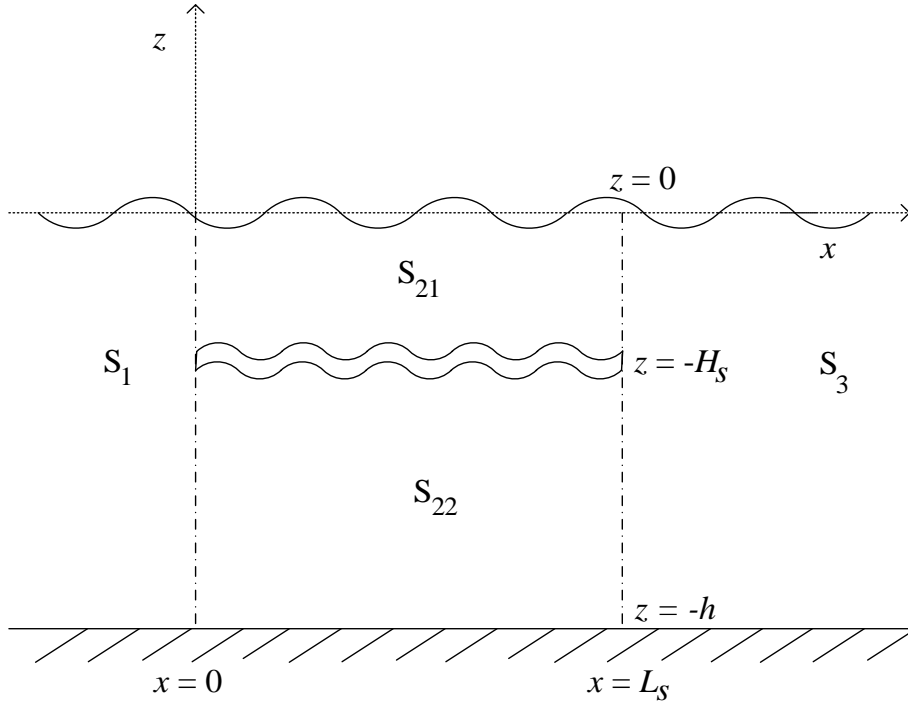


Fig. 11: Schematic diagram for the analysis.

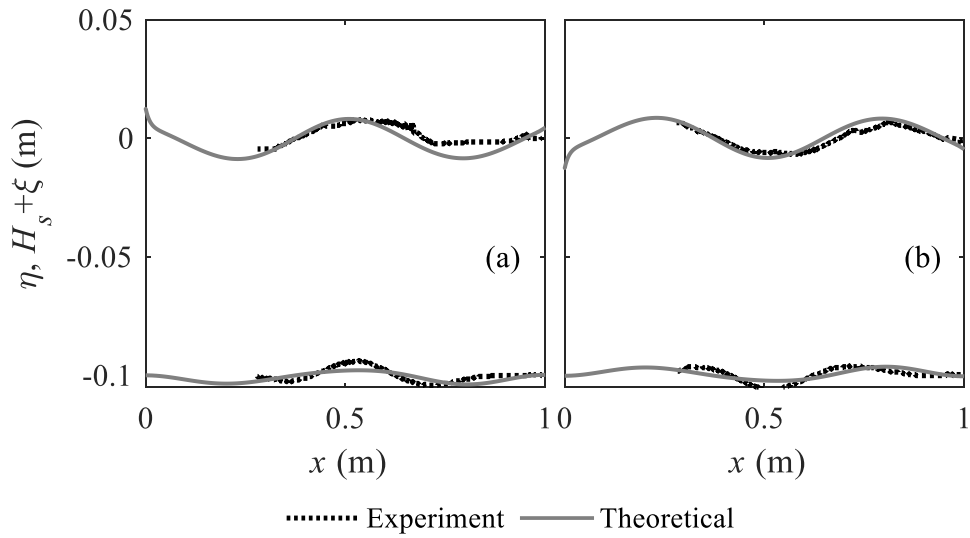


Fig. 12: Comparison of profile between surface wave and submerged sheet profile with experimental data ($T = 0.6$ s, $m_{CA} = 7\%$, and $H_s = 0.1$ m). Profile at (a) $t = 8.73$ s, and (b) $t = 8.73$ s + $T/2$ from the beginning of the experiment.

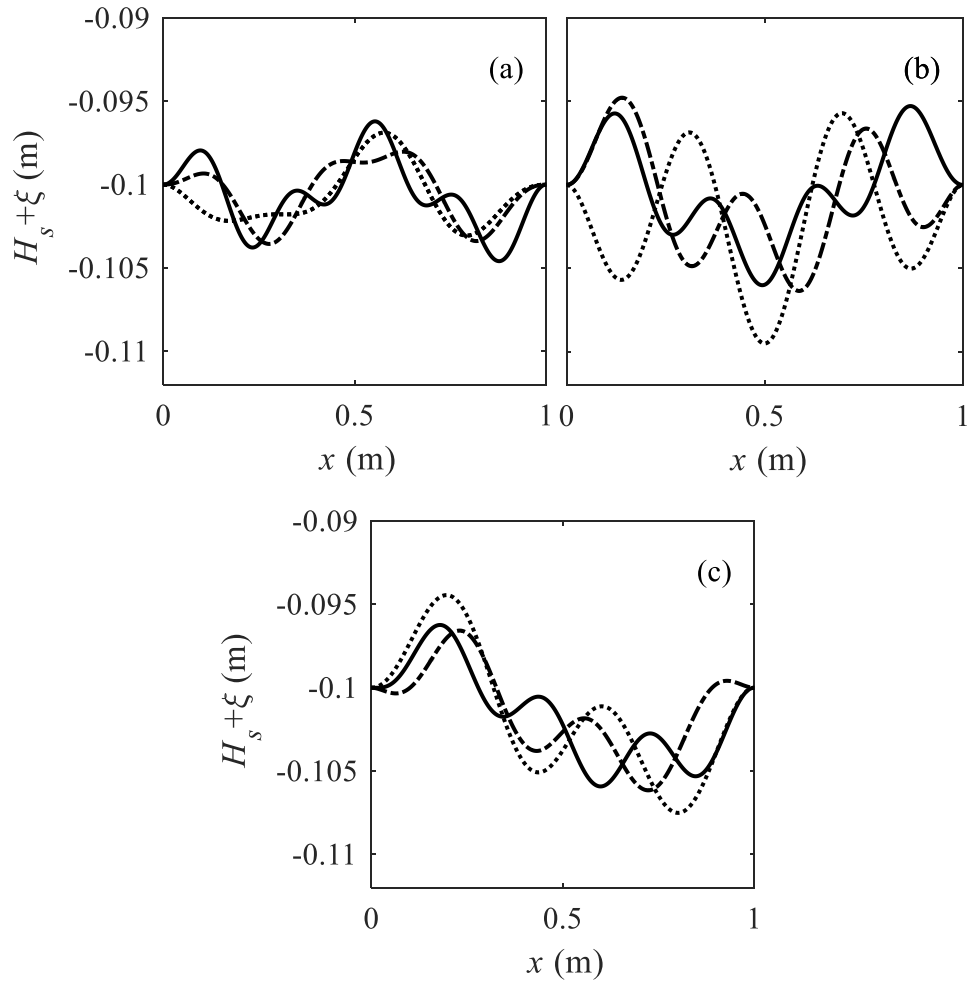


Fig. 13a: Predictions of sheet displacement profile (finite viscosity) at $t = T$. m_{CA} (%): solid line = 4, dash-dot line = 7, and dotted line = 10. T (s): (a) 0.6, (b) 0.8 and (c) 1.0.

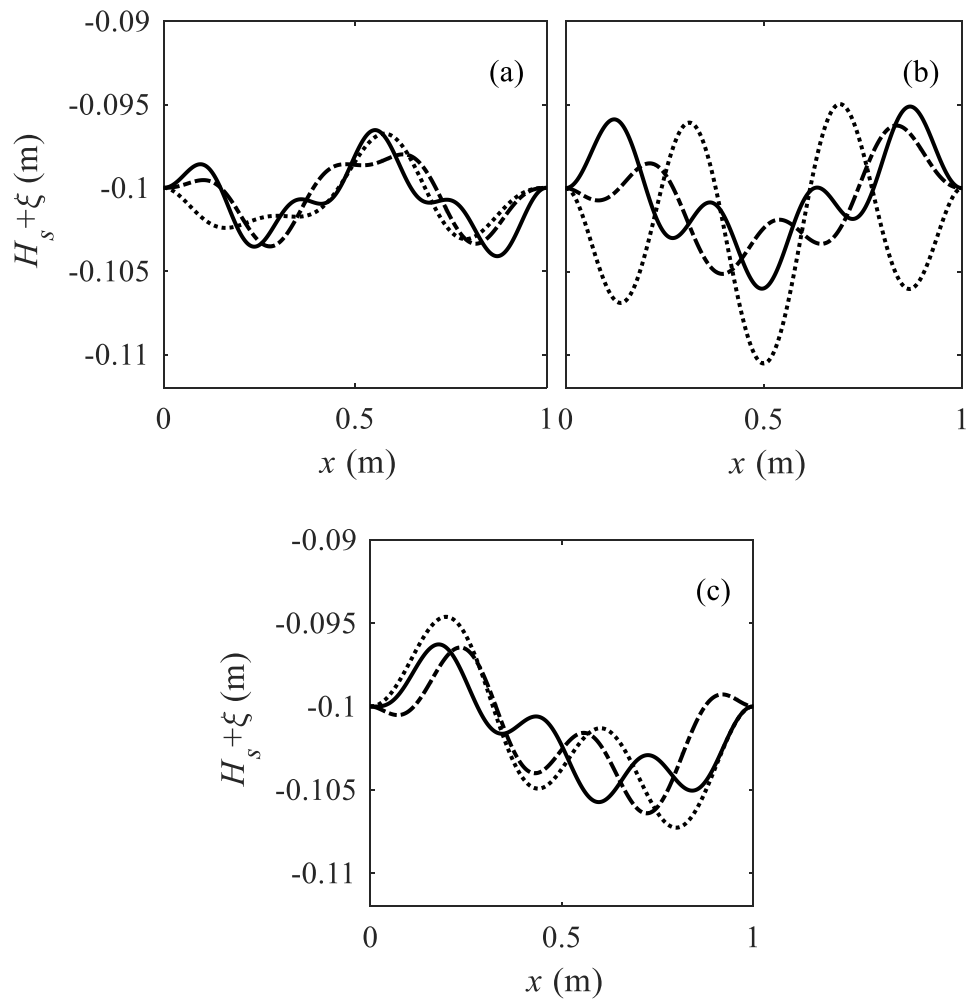


Fig. 13b: Predictions of sheet displacement profile (zero viscosity) at $t = T$. m_{CA} (%): solid line = 4, dash-dot line = 7, and dotted line = 10. T (s): (a) 0.6, (b) 0.8 and (c) 1.0.

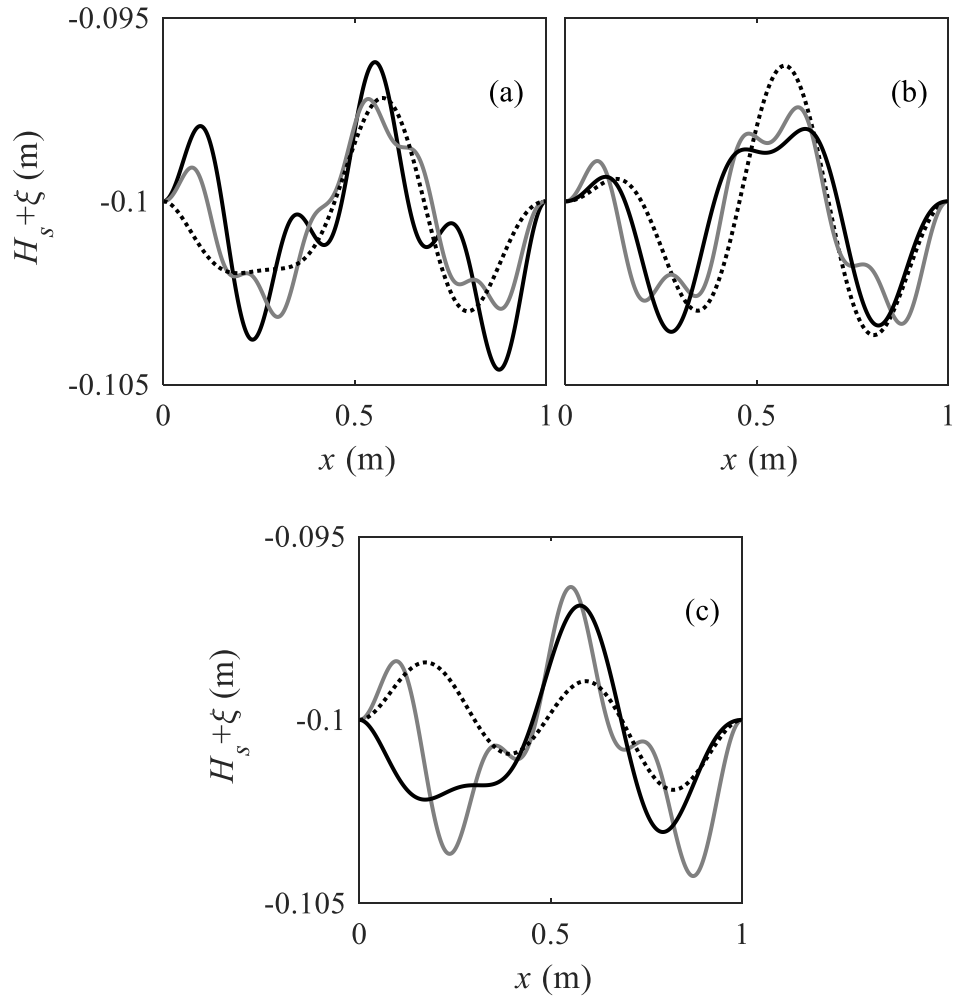


Fig. 14a: Sheet displacement profile with different thickness (finite viscosity) at $t = T = 0.6$
s. m_{CA} (%): (a) 4, (b) 7, and (c) 10. d_s ($\times 10^{-2}$ m): grey solid line = 0.5, black solid line =
1.0 and black dotted line = 2.0.

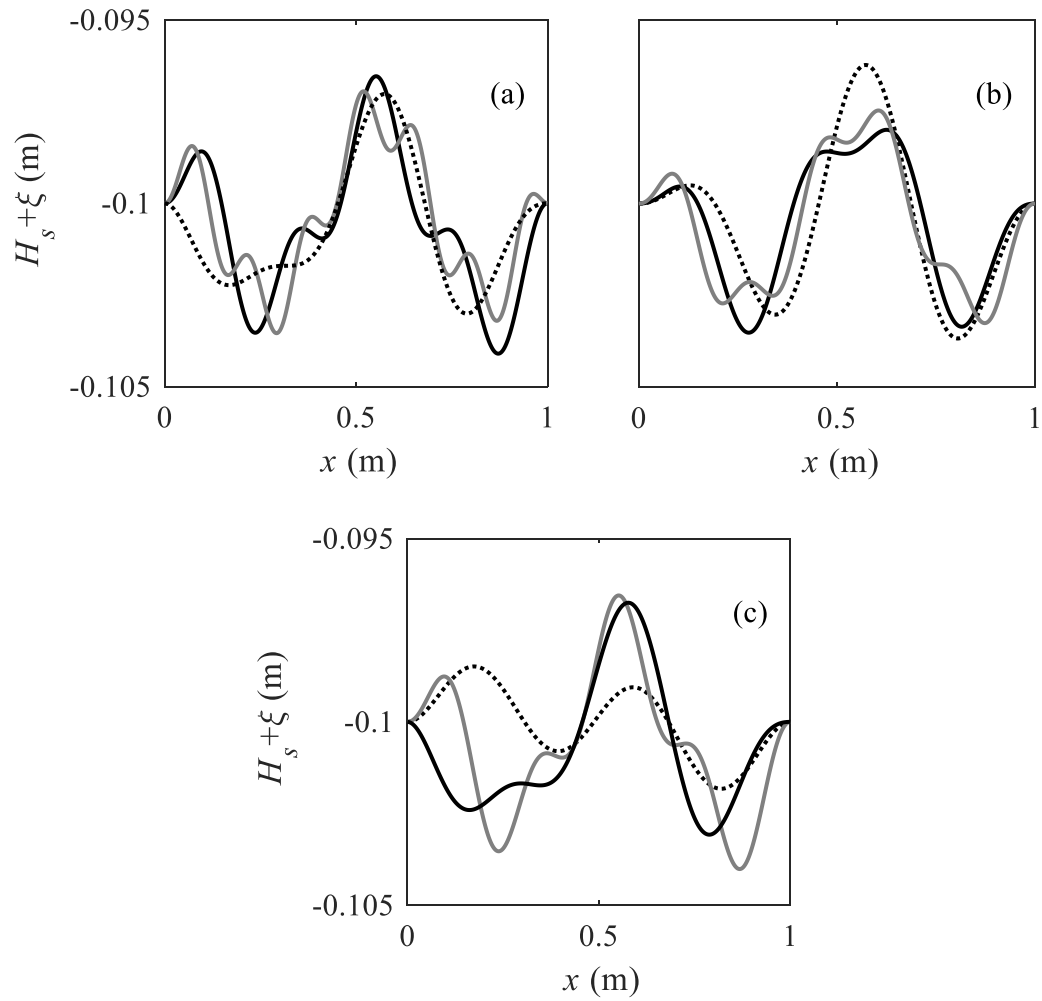


Fig. 14b: Sheet displacement profile with different thickness (zero viscosity) at $t = T = 0.6$ s. m_{CA} (%): (a) 4, (b) 7, and (c) 10. d_s ($\times 10^{-2}$ m): grey solid line = 0.5, black solid line = 1.0 and black dotted line = 2.0.

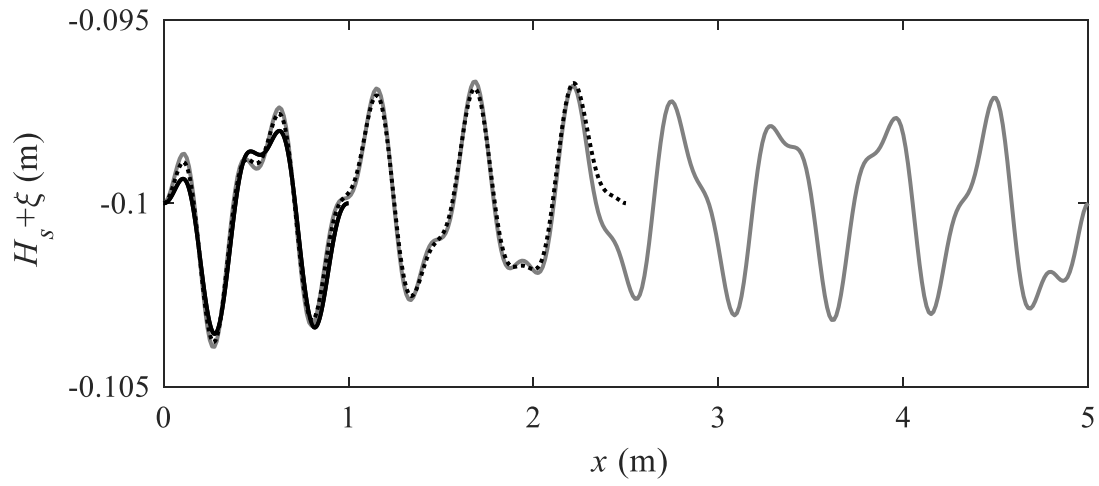


Fig. 15: Sheet displacement profile with different length ($m_{CA} = 7\%$, $d_s = 0.01$ m, $H_s = 0.1$ m) at $t = T = 0.6$ s. L_s (m): black solid line = 1.0, dotted line = 2.5, and grey solid line = 5.0.

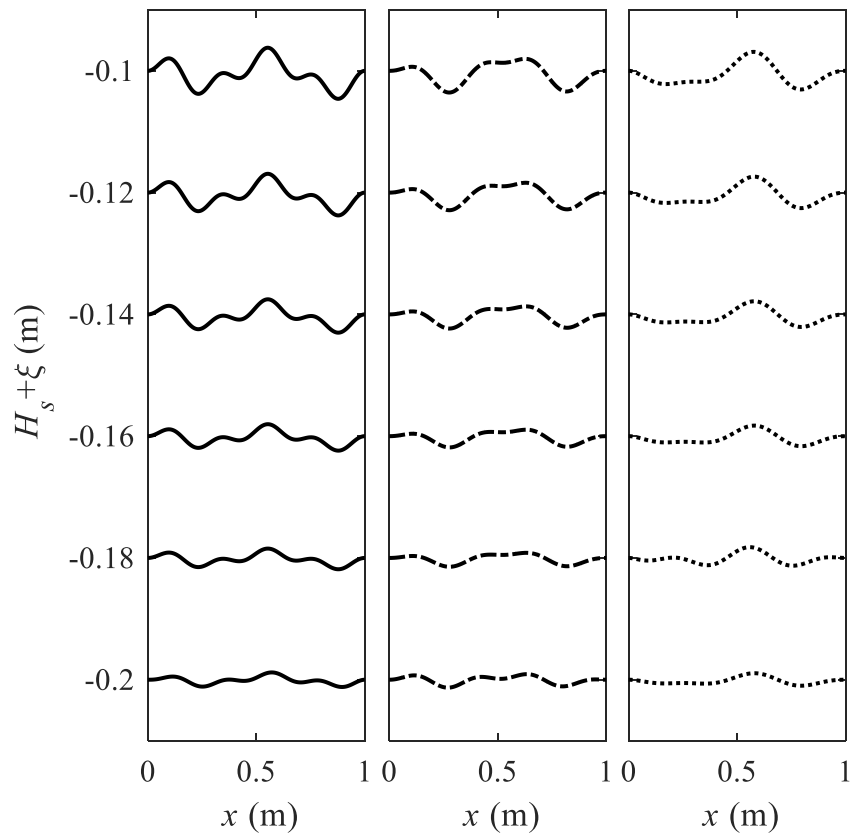


Fig. 16: Sheet displacement profile with different submergences, $d_s = 0.01$ m at $t = T = 0.6$ s. m_{CA} (%): solid line = 4, dash-dot line = 7, and dotted line = 10.

Table 1: Shear modulus and viscosity of oil-doped PDMS sheets based on Voigt model

T (s)	ω (rad/s)	G ($\times 10^4$ Pa)			ν (m^2/s)		
		m_{CA}					
		4%	7%	10%	4%	7%	10%
0.5	12.56	3.86	9.43	27.79	0.22	0.45	1.04
0.6	10.47	3.84	9.37	27.70	0.24	0.51	1.17
0.7	8.97	3.82	9.33	27.59	0.27	0.56	1.29
0.8	7.85	3.80	9.29	27.51	0.29	0.61	1.41
0.9	6.97	3.79	9.26	27.46	0.31	0.66	1.52
1.0	6.28	3.78	9.23	27.42	0.33	0.70	1.62

Table 2: Input wave characteristics.

T (s)	λ (m)	k_o (rad/m)	$k_o A_o$
0.50	0.39	16.08	0.12
0.60	0.56	11.19	0.08
0.70	0.75	8.32	0.06
0.80	0.96	6.53	0.06
0.90	1.17	5.37	0.05
1.00	1.373	4.57	0.04

Table 3: Wave energy reduction for open water case.

T (s)	\tilde{E}_{wL}	\tilde{E}_{wT}	r_e [%]
0.5	0.32 \pm 0.01	0.30 \pm 0.00	5
0.6	0.32 \pm 0.00	0.30 \pm 0.02	5
0.7	0.34 \pm 0.00	0.32 \pm 0.02	5
0.8	0.31 \pm 0.00	0.31 \pm 0.04	0
0.9	0.36 \pm 0.00	0.34 \pm 0.05	4
1.0	0.29 \pm 0.01	0.29 \pm 0.05	0

Table 4: Wave energy reduction due to submerged viscoelastic sheet.

H_s (m)	T (s)	m_{CA} (%): 4%			7%			10%		
		\tilde{E}_{wL}	\tilde{E}_{wT}	r_e %	\tilde{E}_{wL}	\tilde{E}_{wT}	r_e %	\tilde{E}_{wL}	\tilde{E}_{wT}	r_e %
0.10	0.5	0.33±0.01	0.09±0.01	73	0.35±0.01	0.11±0.01	69	0.29±0.09	0.00±0.00	99
	0.6	0.38±0.05	0.11±0.01	72	0.33±0.03	0.22±0.01	32	0.31±0.02	0.17±0.01	46
	0.7	0.40±0.06	0.17±0.01	58	0.36±0.01	0.16±0.01	55	0.31±0.01	0.24±0.01	22
	0.8	0.34±0.04	0.15±0.01	57	0.36±0.08	0.17±0.01	52	0.29±0.03	0.22±0.01	24
	0.9	0.37±0.04	0.23±0.01	38	0.37±0.04	0.23±0.02	37	0.36±0.04	0.22±0.01	39
	1.0	0.31±0.03	0.26±0.02	14	0.27±0.06	0.19±0.04	29	0.29±0.04	0.25±0.03	15
0.075	0.5	0.31±0.01	0.08±0.02	74	0.32±0.01	0.21±0.01	33	0.35±0.03	0.13±0.01	62
	0.6	0.39±0.08	0.05±0.00	88	0.32±0.05	0.15±0.01	52	0.29±0.04	0.21±0.02	28
	0.7	0.42±0.08	0.09±0.01	79	0.35±0.02	0.06±0.01	82	0.31±0.05	0.24±0.01	21
	0.8	0.34±0.04	0.11±0.01	67	0.38±0.08	0.10±0.01	76	0.32±0.08	0.17±0.02	48
	0.9	0.38±0.07	0.16±0.01	58	0.38±0.06	0.19±0.02	47	0.38±0.05	0.17±0.01	52
	1.0	0.30±0.05	0.23±0.02	24	0.27±0.05	0.14±0.04	49	0.28±0.05	0.22±0.03	21
0.05	0.5	0.38±0.01	0.01±0.00	99	0.25±0.01	0.04±0.01	84	0.31±0.02	0.13±0.01	58
	0.6	0.35±0.02	0.08±0.00	78	0.37±0.10	0.05±0.01	86	0.32±0.07	0.04±0.01	89
	0.7	0.33±0.04	0.13±0.00	61	0.36±0.10	0.04±0.01	89	0.33±0.05	0.06±0.01	83
	0.8	0.31±0.04	0.17±0.01	44	0.40±0.07	0.1±0.01	74	0.39±0.09	0.06±0.00	87
	0.9	0.38±0.05	0.17±0.01	55	0.38±0.07	0.12±0.01	69	0.38±0.06	0.10±0.01	74
	1.0	0.32±0.04	0.17±0.01	47	0.27±0.06	0.13±0.04	53	0.26±0.06	0.09±0.01	64